BS 2

LA-10415-MS

KS

Minerals in Fractures of the Unsaturate[illegible] from Drill Core USW G-4, Yucca Mo[illegible] Nye County, [illegible]

Los Alamos National Lab[illegible]
Los Alamos, New Mexic[illegible]

This report was prepared by the Los Alamos National Laboratory as part of the Nevada Nuclear Waste Storage Investigations managed by the Nevada Operations Office of the US Department of Energy. Based upon their applicability to the investigations, some results from the Radionuclide Migration Project, managed by the Nevada Operations Office of the US Department of Energy, are included in this report.

LA-10415-MS

UC-70
Issued: May 1985

Minerals in Fractures of the Unsaturated Zone from Drill Core USW G-4, Yucca Mountain, Nye County, Nevada

B. Arney Carlos

Los Alamos National Laboratory
Los Alamos, New Mexico 87545

MINERALS IN FRACTURES OF THE UNSATURATED ZONE FROM DRILL CORE USW G-4, YUCCA MOUNTAIN, NYE COUNTY, NEVADA

by

B. Arney Carlos

ABSTRACT

The mineralogy of fractures in drill core USW G-4, from a depth of nearly 800 ft to the static water level (SWL) at 1770 ft, was examined to determine the sequence of deposition and the identity of minerals that might be natural barriers to radionuclide migration from a nuclear waste repository. Mordenite was found to be present, though not abundant, at the top of the interval sampled (the top of the lower lithophysal zone of the Topopah Spring Member of the Paintbrush Tuff). Heulandite occurs from about 1245 to 1378 ft; below 1378 ft, clinoptilolite rather than heulandite occurs alone or with mordenite. Smectite in fractures is abundant only in the vitrophyre of the Topopah Spring Member of the Paintbrush Tuff and at the top of the Prow Pass Member of the Crater Flat Tuff.

The unsaturated zone below 800 ft can be divided into three rock types: devitrified, glassy, and zeolitized host rock. Fracture-lining zeolites for each of these three rock types differ in mineralogy and morphology. Similarities between fracture mineralogy and host-rock alteration in the nonwelded zeolitic units of the Topopah Spring Member suggest that this zone was once below the water table. The difference between microcrystalline ($\geq$0.01 mm) fracture coatings in the vitric zone and the mostly cryptocrystalline ($\ll$0.01 mm) fracture coatings in the zeolitic zone also suggests that the conditions under which these two types of linings formed were different. Nonwelded glass shards preserved in the host rock above the zeolite-mineral transition in the fractures indicate that the water table was never higher than the lithic-rich base of the Topopah Spring Member in the vicinity of USW G-4. Fracture linings in the zeolitic Topopah Spring Member are clinoptilolite, but the crystal size (0.01-0.02 mm) is closer to that of heulandite in fractures of the vitric zone above it than to clinoptilolite in the Tuff of Calico Hills below.

I. Introduction

Yucca Mountain, located on the southwest margin of the Nevada Test Site (Fig. 1), is being studied as a potential repository for high-level nuclear waste. These studies are coordinated under the Nevada Nuclear Waste Storage Investigations (NNWSI) Project managed by the Nevada Operations Office of the Department of Energy. The site at Yucca Mountain is within an upthrown block of Miocene volcanic rocks that are 1.5-4 km thick and range in age from 12.5 to 14 Myr (Scott et al., 1983; Marvin et al., 1970; Carr et al., 1984). The area has been mapped by Christiansen and Lipman (1965) and by Lipman and McKay (1965). Detailed descriptions of the ash flow tuffs comprising the mountain are given in Lipman et al. (1966), Byers et al. (1976), and Carr et al. (1984). Stress regimes, regional structure, and fracture abundance and orientation have been discussed by Carr (1974) and by Scott et al. (1983). The importance of fractures as groundwater flow paths, especially through densely welded tuff, was emphasized by Scott et al. (1983), who presented a hydrologic model for fluid flow in the unsaturated zone of Yucca Mountain.

Understanding natural barriers to radionuclide migration is important in evaluating a potential waste repository site. Studies of sorptive minerals such as clays and zeolites along flow paths away from the repository site must include the minerals that line fractures immediately above and below the candidate host rock, as well as along flow paths farther from the repository. Studying the mineralogy in fractures and the similarities and differences between fracture and rock-matrix mineralogy could also provide information about rock-alteration histories and paleo water tables. Alteration histories can be used to predict what might happen in the thermal regime produced by the waste after it is emplaced.

Several holes have been drilled in Yucca Mountain for geologic and hydrologic studies. Drill hole USW G-4, the most recent cored hole within the proposed repository block, was chosen for detailed study of fracture-filling materials because it is closest to the proposed NNWSI exploratory shaft. A study of the fracture minerals in USW G-4 drill core should indicate conditions that can be expected along flow paths within the northeastern part of the repository.

The general stratigraphy of drill hole USW G-4 based on Spengler et al. (1984) is shown in Fig. 2. The unit being considered for a repository is the

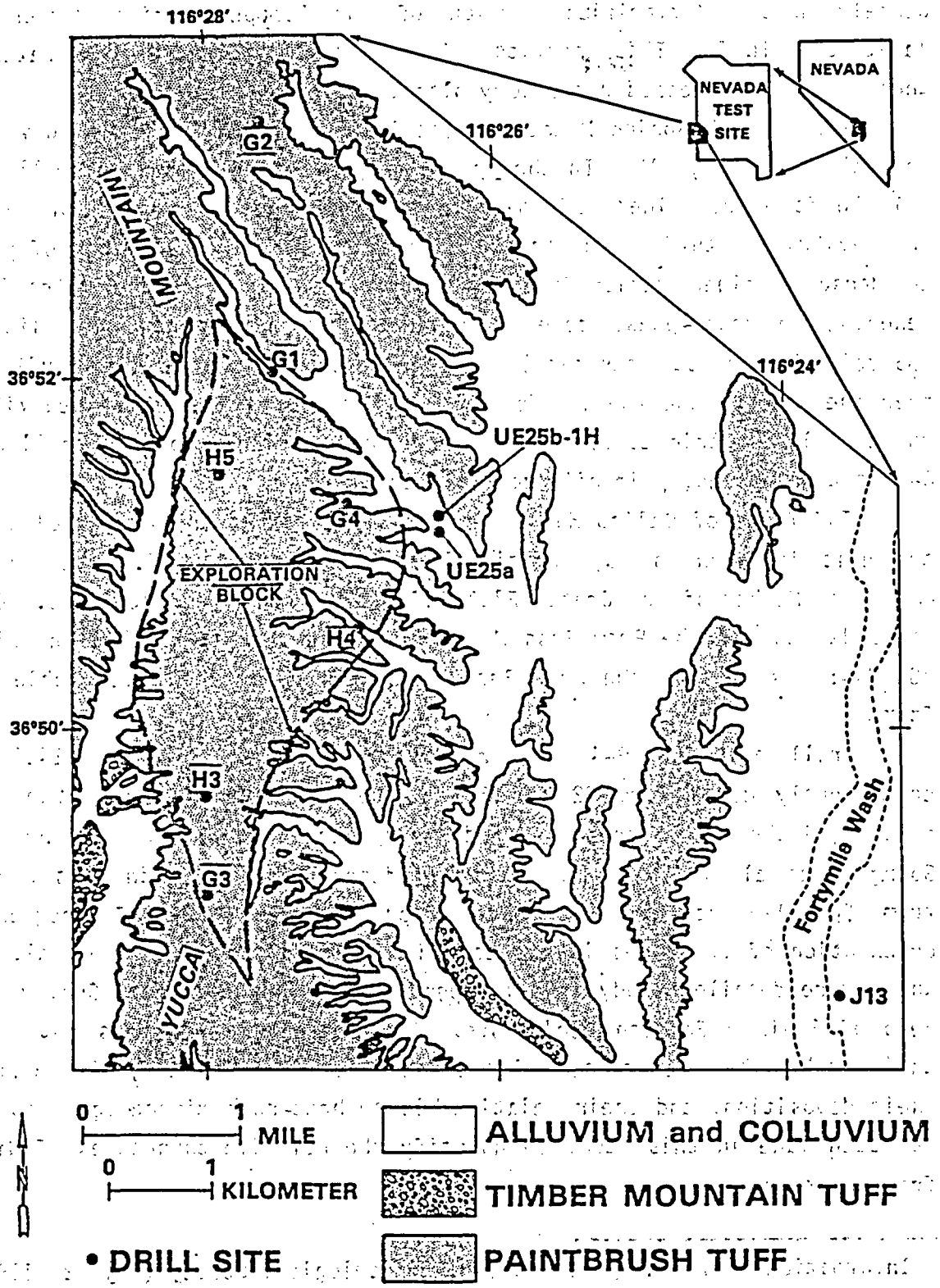

Fig. 1.
Location of Yucca Mountain and drill holes, including USW G-4.

densely welded devitrified portion of the Topopah Spring Member of the Paintbrush Tuff. This portion of the tuff is above the water table throughout the proposed repository block.

The Topopah Spring Member of the Paintbrush Tuff has been divided into several zones (Fig. 2). In the upper Topopah Spring Member in drill hole USW G-4, 10 ft of nonwelded tuff overlie a densely welded caprock of vitrophyre and devitrified tuff. Beneath the caprock is a vapor-phase zone of partially to densely welded devitrified tuff. The densely welded devitrified tuff beneath the vapor-phase zone is divided into upper and lower lithophysal ($\geq$5 vol% lithophysal cavities) and nonlithophysal zones. The vitric zone near the base of the Topopah Spring Member includes densely welded vitrophyre and nonwelded vitric tuff. The basal Topopah Spring Member in drill hole USW G-4 is a nonwelded, primarily zeolitic tuff.

The Tuffs of Calico Hills are zeolitic, bedded and nonwelded tuffs and the unit is underlain by additional zeolitic bedded tuff. The top of the Prow Pass Member of the Crater Flat Tuff is nonwelded and zeolitic. Only the nonwelded top of the Prow Pass Member is above the water table in drill hole USW G-4; the rest of the Prow Pass Member is below the water table at 1770 ft.*

Drill hole USW G-4 was drilled in 1982 to 3001 ft (914.7 m) and continuously cored from 22 ft (6.7 m) to total depth (TD). The drilling history, lithology of the core, and geophysical logs of the well are given in Spengler et al. (1984). Stratigraphic descriptions used in this report are from Spengler et al. (1984). A preliminary study of frequency and orientation of fractures in the core is included in Spengler et al. (1984), and a more detailed study is being performed by US Geological Survey with the help of Fenix & Scisson geologists. The present report does not duplicate their work but is concerned with fracture-lining minerals, the sequence of their deposition, and their relationship to host-rock mineralogy. No attempt has been made in this study to quantify the relative abundances of different fracture types.

---

* Information provided by J. Robison, US Geological Survey (May 22, 1984).

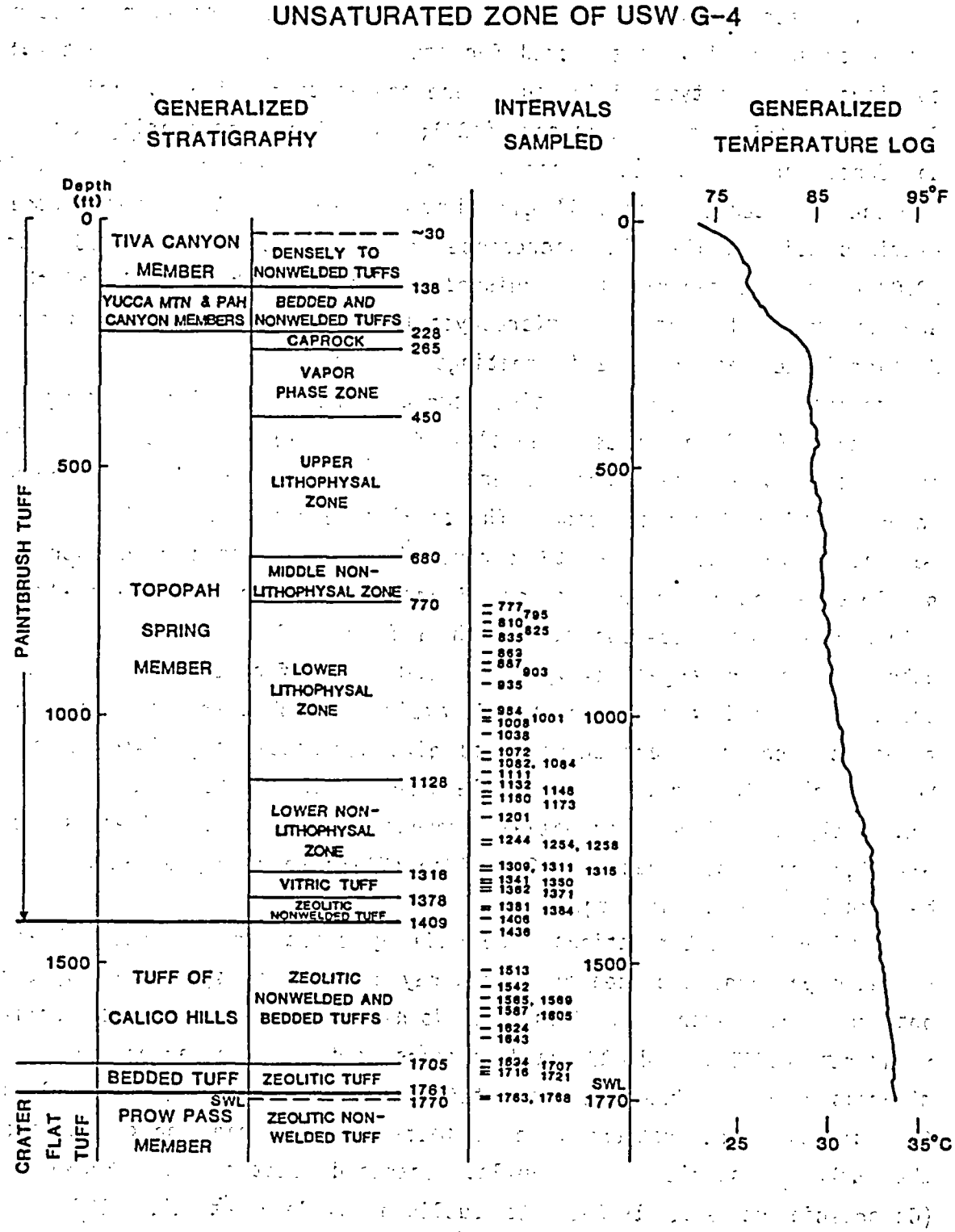

Fig. 2.
Generalized stratigraphy (from Spengler et al., 1984), intervals sampled, temperature log (Birdwell Div., Seismograph Service Corp., Nov. 30, 1982), and static water level (SWL) [J. Robison, US Geological Survey (1984)] in USW G-4.

II. Methods

Representative core samples for each interval and each fracture type within an interval were selected for study. Samples with the most extensive coatings for each type of fracture were chosen to provide sufficient material for x-ray diffraction analysis (XRD); therefore, estimating the mineral abundances in all fractures based on the surface coverage listed in Table I for the selected samples will give invalid results. All samples were first examined using a binocular microscope (50x magnification). At 50x, crystals $\geq$0.02 mm can be clearly distinguished. Coatings with crystals of this size are therefore described as microcrystalline. Crystals $\leq$0.01 mm cannot be distinguished at 50x and coatings of this size are described as cryptocrystalline. Representative samples were chosen for scanning electron microscope (SEM) analyses. Samples for XRD were scraped from fracture surfaces with a steel scraper, and the scraped materials were hand-picked under the binocular microscope. The samples were then crushed to powder in a ceramic mortar and exposed to x rays either as pressed powder or as smear samples, depending on the amount of material available. XRD patterns were obtained in the step-scan mode with a Siemens D-500 powder diffractometer using a copper-target x-ray tube and a diffracted-beam monochromator. Because of the different amounts of sample obtainable from each fracture, the times at each step were adjusted to give acceptable signal-to-noise ratios. Some samples that gave questionable results at shorter scan rates or that apparently contained substantial amounts of manganese minerals were run overnight at a scan rate of 12 min/deg (2θ); other samples were analyzed at between 1.6 and 4.2 min/deg.

Mineral identifications were made by comparing observed patterns with standard patterns produced by this x-ray diffraction system and by comparing patterns with standards from the Joint Committee on Powder Diffraction Standards (JCPDS). JCPDS card numbers and the characteristic peaks of minerals found in Yucca Mountain tuffs were reported by Bish et al. (1981). The mineral concentrations were estimated by comparing peak intensities of the unknown samples with in-lab standard patterns of known mixtures (Caporuscio et al., 1982). As outlined in Bish et al. (1981), several assumptions are implicit in such estimates, including an assumed lack of significant preferred orientation and of appreciable variations in intensity

TABLE I
X-RAY DIFFRACTION ANALYSES OF FRACTURE FILLINGS USW G-4 UNSATURATED ZONE

Unit	Sample	Estimated Fracture Surface Coated %	Estimated Max. Rock Contamination %	Smectite	Clinoptilolite/ Heulandite	Mordenite	Quartz	Cristobalite	Alkali Feldspar	Tridymite
Topopah Spring Member										
Lower Lithophysal Zone	810	40	5	21 ± 5	--	61 ± 10	18 ± 3	--	--	--
	887	90	30	2 ± 1	--	--	12 ± 2	5 ± 3	74 ± 10	7 ± 4
	984	100	20	--	--	--	79 ± 5	<1	14 ± 5	6 ± 3
	1001	10	40	<1	--	--	21 ± 4	5 ± 3	73 ± 10	--
	1008	100	15	<1	--	11 ± 5	40 ± 5	10 ± 5	39 ± 10	--
	1033 X	100	20	15 ± 5	--	--	24 ± 8	5 ± 3	36 ± 10	20 ± 5
	1072 #1	100	30	--	--	--	65 ± 5	<1	22 ± 10	12 ± 4
	1072 #2	30	30	<1	--	7 ± 4	17 ± 1	10 ± 4	55 ± 10	10 ± 4
	1093 #3	90	10	6 ± 2	--	--	9 ± 2	5 ± 3	66 ± 10	14 ± 5
Welded Devitrified "Candidate Host Rock"	1160	50	10	--	--	--	33 ± 5	7 ± 4	60 ± 10	--
	1173	25	10	3 ± 1	--	52 ± 15	32 ± 8	14 ± 5	--	--
	1201	95	50	--	--	--	56 ± 10	6 ± 4	37 ± 10	--
	1244	60	15	<1	--	--	40 ± 5	8 ± 4	51 ± 10	--
	1254 #1	100	15	--	48 ± 10	12 ± 5	18 ± 2	14 ± 5	8 ± 4	--
	1254 #3	100	10	--	47 ± 10 H	10 ± 5	17 ± 3	12 ± 4	14 ± 6	--
	1258	100	5	7 ± 3	29 ± 5	--	12 ± 3	7 ± 4	45 ± 10	--
	1309	90	5	--	100 H	--	--	--	--	--
Vitrophyre	1341 blue	100	50	7 ± 3	57 ± 20	--	--	36 ± 15	--	--
	1341 cream	100	10	62 ± 10	33 ± 10	--	--	5 ± 3	--	--
	1341 beige	35	10	4 ± 2	82 ± 10 H	14 ± 5	--	--	--	--
Vitric Tuff	1350	100	20	10 ± 5	90 ± 10 H	--	--	--	--	--
	1362	20	>50	8 ± 3	36 ± 15	25 ± 10	--	11 ± 4	12 ± 8	8 ± 4
Zeolitic Non-welded Tuff	1381	100	50	<1	58 ± 10 C	--	5 ± 3	7 ± 4	--	29 ± 10
Tuffs of Calico Hills										
	1436	100	20	--	100 C	--	--	--	--	--
Zeolitic Nonwelded and Bedded Tuffs	1513	100	20	--	55 ± 10	13 ± 10	11 ± 5	8 ± 4	--	8 ± 3
	1542	100	15	2 ± 1	64 ± 10	24 ± 10	7 ± 2	3 ± 2	--	--
	1643	100	20	--	29 ± 10	71 ± 10	--	--	--	--
	1694	Not readily discernible from rock matrix		2 ± 1	56 ± 10	21 ± 10	10 ± 3	5 ± 3	--	6 ± 3
Zeolitic Bedded Tuff	1707	70	10	--	21 ± 10	79 ± 10	--	--	--	--
	1716	30	50	10 ± 5	41 ± 10	23 ± 10	21 ± 4	2 ± 1	--	3 ± 2
Prow Pass Member										
Zeolitic Nonwelded Tuff	1763 white	100	Not determined; intergrown with rock grains	88 ± 10	8 ± 3	--	--	4 ± 2	--	--
	1763 orange	100		68 ± 10	22 ± 10	5 ± 3	<1	4 ± 3	--	--

SWL

-- = None detected.

with compositional changes. Small amounts of sample often required using smear samples or small-cavity glass slides rather than the larger-cavity glass slides. Some particles were unavoidably oriented during this process. Intensity humps in the XRD patterns of several samples resulted from x rays reflecting off the glass slide and from contamination from the vitric host rock. Estimating intensity of XRD peaks from such samples was difficult. Because of these analytical difficulties and the overlapping XRD peaks of the minerals in each sample, the concentrations in Table I, particularly those for alkali feldspar in the presence of mordenite, have sizable uncertainties.

Samples of heulandite-clinoptilolite were heated overnight at 450°C and x-rayed again. At this temperature, the heulandite structure breaks down but clinoptilolite is stable (Mumpton, 1960). Clay separates were obtained by differential settling in water from samples with sufficient smectite ($\geq$50% for the small amounts of material obtained from fractures), glycolated, and x-rayed again to determine the amount of illite/smectite interstratification.

Thin sections of samples that had sealed fractures were made for microprobe analysis. Making thin sections across most open fractures was impossible because of differential grinding of the softer fracture-filling minerals. Elemental compositions of minerals were determined on an automated Cameca electron microprobe with accelerating potential fixed at 15 kV and a sample current of 15 μA on thorium oxide. Analyses were made at either 10 s or 30 000 counts for each element. Compositions were calculated from corrected peak intensities using the methods of Bence and Albee (1968). Feldspar standards were used for the zeolite analyses. The Bence-Albee corrections are thus based on a dense, anhydrous tectosilicate structure (feldspar) with assumed absorption/fluorescence of the returning X rays from the sample based on that structure. The zeolite structure contains considerable void space that is normally filled with water that vaporizes during the analysis. For this reason, zeolite analyses using feldspar standards and Bence-Albee corrections not only have low totals but also may yield cation ratios that are not as accurate as those for most anhydrous silicates. Some sodium migration (Graham et al., 1984) was unavoidable. Because most crystals were small, a small raster had to be used, and the beam often could not be moved to new areas of the crystal during analysis. Most of the analyses probably indicate slightly less sodium than is actually present. Zeolite analyses given in Table II and cation ratios discussed in

TABLE II

MICROPROBE ANALYSES OF FRACTURE-LINING ZEOLITES IN THE UNSATURATED ZONE OF DRILL CORE USW G-4

A. Compositions of Heulandite in Fractures

Depth	1258				1309						1311						1341			
SiO2	62.44	64.81	63.23	62.32	62.05	59.77	61.35	61.78	62.67	63.14	60.34	61.19	63.66	62.24	61.93	61.43	51.73	58.00	57.83	49.68
TiO2	0.04	0.04	0.03	0.02	0.00	0.10	0.04	0.00	0.00	0.03	0.00	0.00	0.00	0.00	0.00	0.00	0.16	0.03	0.13	0.00
Al2O3	14.31	14.62	14.36	14.26	13.71	13.54	12.64	14.04	14.14	14.28	13.12	13.06	12.42	13.41	13.14	13.20	11.38	12.23	13.00	11.94
Fe2O3	0.00	0.03	0.02	0.00	0.00	0.03	0.05	0.00	0.00	0.05	0.00	0.00	0.03	0.00	0.00	0.00	0.45	0.09	0.23	0.27
MgO	1.35	1.31	1.29	1.51	0.85	1.26	0.78	1.29	1.39	1.31	0.55	0.01	0.13	0.07	0.13	0.55	0.03	0.00	0.12	0.11
CaO	4.72	4.65	4.75	4.60	5.47	4.95	5.11	5.01	5.14	5.13	5.33	5.63	5.47	5.63	5.50	4.97	4.06	4.50	4.44	3.66
BaO	0.00	0.09	0.03	0.05	0.12	0.03	0.09	0.00	0.05	0.09	0.16	0.16	0.03	0.10	0.17	0.06	0.14	0.02	0.00	0.11
Na2O	0.33	0.35	0.32	0.17	0.18	0.20	0.13	0.25	0.31	0.21	0.22	0.91	0.23	0.99	0.84	0.78	0.93	0.94	1.09	1.89
K2O	0.34	0.53	0.28	0.26	0.37	0.34	0.26	0.28	0.33	0.27	0.44	0.41	0.61	0.46	0.59	0.49	0.95	1.74	1.20	1.16
Total	83.53	86.43	84.31	83.19	82.75	80.22	80.45	82.65	84.03	84.51	80.16	81.37	82.58	82.90	82.35	81.48	69.83	77.55	78.04	68.82
Cation Formulae																				
Si	28.48	28.59	28.55	28.50	28.65	29.45	29.03	28.50	28.48	28.50	28.78	28.85	29.38	28.80	28.86	28.83	28.59	28.87	28.55	28.06
Ti	0.01	0.01	0.01	0.01	0.00	0.04	0.01	0.00	0.00	0.01	0.00	0.00	0.00	0.00	0.00	0.00	0.07	0.01	0.05	0.00
Al	7.70	7.60	7.65	7.69	7.46	7.60	7.05	7.63	7.58	7.60	7.38	7.26	6.76	7.31	7.22	7.30	7.41	7.18	7.57	7.95
Fe	0.00	0.01	0.01	0.00	0.00	0.01	0.02	0.00	0.00	0.02	0.00	0.00	0.01	0.00	0.00	0.00	0.19	0.03	0.09	0.11
Mg	0.92	0.86	0.87	1.03	0.58	0.89	0.55	0.89	0.94	0.88	0.39	0.01	0.09	0.05	0.13	0.38	0.02	0.00	0.09	0.09
Ca	2.31	2.20	2.30	2.25	2.71	2.52	2.59	2.48	2.50	2.48	2.72	2.84	2.71	2.79	2.75	2.50	2.40	2.40	2.35	2.21
Ba	0.00	0.02	0.01	0.01	0.02	0.01	0.02	0.00	0.01	0.02	0.03	0.03	0.01	0.02	0.03	0.01	0.03	0.00	0.00	0.02
Na	0.29	0.30	0.28	0.15	0.16	0.18	0.12	0.22	0.27	0.18	0.20	0.83	0.21	0.89	0.76	0.71	1.00	0.91	1.04	2.07
K	0.20	0.30	0.16	0.15	0.22	0.21	0.16	0.16	0.19	0.16	0.27	0.25	0.36	0.27	0.35	0.29	0.67	1.11	0.76	0.84
Coordination of Cations																				
Tet.	36.19	36.22	36.22	36.20	36.11	36.09	36.12	36.13	36.05	36.13	36.15	36.11	36.15	36.11	36.08	36.13	36.25	36.10	36.24	36.12
Other	3.71	3.67	3.61	3.60	3.69	3.81	3.43	3.75	3.92	3.72	3.62	3.96	3.37	4.02	4.01	3.90	4.13	4.42	4.24	5.24
Ratio of Si to Al+Fe																				
	3.70	3.76	3.73	3.71	3.84	3.74	4.11	3.73	3.76	3.74	3.90	3.97	4.34	3.94	4.00	3.95	3.76	4.00	3.73	3.48
Al+Fe/2Mg+2Ca+2Ba+Na+K																				
	1.11	1.13	1.13	1.12	1.07	1.05	1.07	1.07	1.03	1.07	1.09	1.06	1.10	1.06	1.04	1.08	1.15	1.06	1.15	1.07
Mol.% Potassium,Sodium,and Calcium plus Magnesium																				
K	5.3	8.2	4.5	4.2	5.9	5.4	4.6	4.4	4.9	4.2	7.5	6.3	10.7	6.8	8.8	7.5	16.4	25.0	17.8	16.0
Na	7.9	8.2	7.8	4.2	4.4	4.8	3.5	6.0	7.0	5.0	5.7	21.2	6.1	22.2	19.1	18.3	24.3	20.6	24.6	39.7
Ca+Mg	86.8	83.7	87.8	91.6	89.7	89.7	91.9	89.6	88.1	90.8	86.9	72.6	83.2	71.0	72.1	74.2	59.3	54.4	57.5	44.3
Oxides Recalculated to 100%																				
SiO2	74.75	74.99	75.00	74.91	74.98	74.51	76.26	74.75	74.58	74.71	75.27	75.20	77.09	75.08	75.20	75.39	74.08	74.79	74.10	72.19
TiO2	0.05	0.05	0.04	0.02	0.00	0.12	0.05	0.00	0.00	0.04	0.00	0.00	0.00	0.00	0.00	0.00	0.23	0.04	0.17	0.00
Al2O3	17.13	16.92	17.03	17.14	16.57	16.88	15.71	16.99	16.83	16.90	16.37	16.05	15.04	16.18	15.96	16.20	16.30	15.77	16.66	17.35
Fe2O3	0.00	0.03	0.02	0.00	0.00	0.04	0.06	0.00	0.00	0.06	0.00	0.00	0.04	0.00	0.00	0.00	0.64	0.12	0.29	0.39
MgO	1.62	1.52	1.53	1.82	1.03	1.57	0.97	1.56	1.65	1.55	0.69	0.01	0.16	0.08	0.22	0.68	0.04	0.00	0.15	0.16
CaO	5.65	5.38	5.63	5.53	6.61	6.17	6.35	6.06	6.12	6.07	6.65	6.92	6.62	6.79	6.68	6.10	5.81	5.80	5.69	5.32
BaO	0.00	0.10	0.04	0.06	0.15	0.04	0.11	0.00	0.06	0.11	0.20	0.20	0.04	0.12	0.21	0.07	0.20	0.03	0.00	0.16
Na2O	0.40	0.40	0.38	0.20	0.22	0.25	0.16	0.30	0.37	0.25	0.27	1.12	0.28	1.19	1.02	0.96	1.33	1.21	1.40	2.75
K2O	0.41	0.61	0.33	0.31	0.45	0.42	0.32	0.34	0.39	0.32	0.55	0.50	0.74	0.55	0.72	0.60	1.36	2.24	1.54	1.69

TABLE II (cont)

B. Compositions of Clinoptilolite in Fractures

Depth	1381								1384	1436					
SiO2	65.22	66.06	65.35	67.09	66.19	65.89	66.36	66.04	68.37	67.02	67.33	67.53	67.38	67.94	68.69
TiO2	0.01	0.00	0.00	0.01	0.03	0.01	0.00	0.00	0.00	0.03	0.03	0.01	0.03	0.02	0.02
Al2O3	13.21	13.30	12.96	12.94	13.07	12.76	13.07	13.32	11.60	12.01	11.76	12.94	12.10	12.33	12.16
Fe2O3	0.11	0.12	0.00	0.11	0.06	0.07	0.06	0.02	0.00	0.00	0.03	0.00	0.00	0.00	0.00
MgO	0.00	0.00	0.00	0.00	0.00	0.01	0.00	0.00	0.00	0.01	0.01	0.00	0.02	0.02	0.00
CaO	2.53	2.36	2.63	2.24	2.44	2.23	2.40	2.46	1.85	0.99	0.92	1.25	1.08	1.04	0.90
BaO	0.00	0.09	0.00	0.00	0.00	0.00	0.00	0.02	0.09	0.00	0.00	0.03	0.00	0.00	0.03
Na2O	2.35	2.29	2.22	2.26	2.45	2.31	2.38	2.15	1.56	2.81	2.86	2.74	2.86	2.79	2.68
K2O	4.45	4.36	4.05	4.51	4.48	4.73	3.89	4.43	4.13	5.54	5.27	5.25	5.45	5.16	5.71
Total	87.88	88.58	87.21	89.16	88.72	88.01	88.16	88.44	87.60	88.41	88.21	89.75	88.92	89.30	90.19
Cation Formulae															
Si	29.03	29.12	29.19	29.33	29.16	29.27	29.27	29.13	30.12	29.67	29.80	29.41	29.65	29.67	29.77
Ti	0.00	0.00	0.00	0.00	0.01	0.00	0.00	0.00	0.00	0.01	0.01	0.00	0.01	0.01	0.01
Al	6.93	6.91	6.83	6.67	6.79	6.68	6.80	6.93	6.03	6.27	6.14	6.64	6.28	6.35	6.21
Fe	0.04	0.04	0.00	0.04	0.02	0.02	0.02	0.01	0.00	0.00	0.01	0.00	0.00	0.00	0.00
Mg	0.00	0.00	0.00	0.00	0.00	0.01	0.00	0.00	0.00	0.01	0.01	0.00	0.01	0.01	0.00
Ca	1.21	1.11	1.26	1.05	1.15	1.06	1.13	1.16	0.87	0.47	0.44	0.58	0.51	0.49	0.42
Ba	0.00	0.02	0.00	0.00	0.00	0.00	0.00	0.00	0.02	0.00	0.00	0.01	0.00	0.00	0.01
Na	2.03	1.96	1.92	1.92	2.09	1.99	2.04	1.84	1.33	2.41	2.45	2.31	2.44	2.36	2.25
K	2.53	2.45	2.31	2.52	2.52	2.68	2.19	2.49	2.32	3.13	2.98	2.92	3.06	2.88	3.16
Coordination of Cations															
Tet.	36.00	36.07	36.02	36.04	35.97	35.98	36.08	36.07	36.15	35.94	35.96	36.06	35.93	36.03	35.99
Other	5.76	5.54	5.49	5.48	5.76	5.74	5.36	5.50	4.54	6.02	5.87	5.82	6.02	5.74	5.83
Ratio of Si to Al+Fe															
	4.17	4.19	4.28	4.37	4.28	4.36	4.29	4.20	5.00	4.73	4.85	4.43	4.72	4.67	4.79
Al+Fe/2Mg+2Ca+2Ba+Na+K															
	1.00	1.04	1.01	1.03	0.98	0.99	1.05	1.04	1.11	0.97	0.97	1.04	0.96	1.02	0.99
Mol.% Potassium, Sodium, and Calcium plus Magnesium															
K	43.9	44.4	42.0	45.9	43.7	46.7	40.8	45.4	51.3	52.0	50.7	50.2	50.8	50.1	54.2
Na	35.2	35.4	35.0	35.0	36.3	34.7	38.0	33.5	29.4	40.1	41.8	39.8	40.5	41.2	38.6
Ca+Mg	20.9	20.2	22.9	19.1	20.0	18.6	21.2	21.2	19.3	7.9	7.5	10.0	8.7	8.7	7.2
Oxides Recalculated to 100%															
SiO2	74.21	74.58	74.93	75.25	74.61	74.87	75.27	74.67	78.05	75.81	76.33	75.24	75.78	76.08	76.16
TiO2	0.01	0.00	0.00	0.01	0.03	0.01	0.00	0.00	0.00	0.03	0.03	0.01	0.03	0.02	0.02
Al2O3	15.03	15.01	14.86	14.51	14.73	14.50	14.83	15.06	13.24	13.58	13.33	14.42	13.61	13.81	13.48
Fe2O3	0.13	0.14	0.00	0.12	0.07	0.08	0.07	0.02	0.00	0.00	0.03	0.00	0.00	0.00	0.00
MgO	0.00	0.00	0.00	0.00	0.00	0.01	0.00	0.00	0.00	0.01	0.01	0.00	0.02	0.02	0.00
CaO	2.88	2.66	3.02	2.51	2.75	2.53	2.72	2.78	2.11	1.12	1.04	1.39	1.21	1.16	1.00
BaO	0.00	0.10	0.00	0.00	0.00	0.00	0.00	0.02	0.10	0.00	0.00	0.03	0.00	0.00	0.03
Na2O	2.67	2.59	2.55	2.53	2.76	2.62	2.70	2.43	1.78	3.18	3.24	3.05	3.22	3.12	2.97
K2O	5.06	4.92	4.64	5.06	5.05	5.37	4.41	5.01	4.71	6.27	5.97	5.85	6.13	5.78	6.33

TABLE II (cont)

B. Compositions of Clinoptilolites (cont)

Depth	1436							1763		
SiO2	66.88	57.68	68.22	67.93	67.31	67.38	67.27	69.84	68.47	69.20
TiO2	0.04	0.00	0.02	0.05	0.03	0.03	0.04	0.00	0.00	0.00
Al2O3	12.05	10.78	12.42	11.66	12.34	12.06	12.48	13.79	13.34	13.66
Fe2O3	0.00	0.00	0.00	0.00	0.00	0.00	0.00	0.00	0.09	0.02
MgO	0.00	0.00	0.02	0.00	0.01	0.00	0.00	0.15	0.13	0.14
CaO	1.15	1.02	1.01	0.92	1.04	1.08	1.30	1.88	1.80	1.89
BaO	0.02	0.00	0.10	0.00	0.05	0.00	0.00	0.00	0.07	0.03
Na2O	2.92	2.54	2.59	2.63	2.63	2.87	2.81	3.56	2.94	3.37
K2O	5.29	4.90	5.46	5.56	5.41	5.26	4.89	3.77	3.48	2.99
Total	88.35	76.92	89.84	88.75	88.82	88.68	88.79	92.99	90.32	91.30
Cation Formulae										
Si	29.62	29.43	29.66	29.89	29.62	29.69	29.55	29.21	29.37	29.31
Ti	0.01	0.00	0.01	0.02	0.01	0.01	0.01	0.00	0.00	0.00
Al	6.29	6.49	6.37	6.05	6.40	6.26	6.46	6.80	6.75	6.82
Fe	0.00	0.00	0.00	0.00	0.00	0.00	0.00	0.00	0.03	0.01
Mg	0.00	0.00	0.01	0.00	0.01	0.00	0.00	0.09	0.08	0.09
Ca	0.55	0.56	0.47	0.43	0.49	0.51	0.61	0.84	0.83	0.86
Ba	0.00	0.00	0.02	0.00	0.01	0.00	0.00	0.00	0.01	0.00
Na	2.51	2.51	2.18	2.24	2.24	2.45	2.39	2.89	2.45	2.77
K	2.99	3.19	3.03	3.12	3.04	2.96	2.74	2.01	1.90	1.62
Coordination of Cations										
Tet.	35.92	35.92	36.04	35.95	36.03	35.96	36.03	36.01	36.15	36.14
Other	6.05	6.26	5.71	5.80	5.79	5.92	5.75	5.83	5.27	5.33
Ratio of Si to Al+Fe										
	4.71	4.54	4.66	4.94	4.63	4.74	4.57	4.30	4.33	4.29
Al+Fe/2Mg+2Ca+2Ba+Na+K										
	0.95	0.95	1.02	0.97	1.02	0.97	1.02	1.00	1.09	1.09
Mol.% Potassium,Sodium,and Calcium plus Magnesium										
K	49.5	51.0	53.2	53.8	52.6	50.0	47.7	34.5	36.2	30.3
Na	41.5	40.1	38.3	38.7	38.8	41.4	41.7	49.5	46.5	51.9
Ca+Mg	9.0	8.9	8.5	7.5	8.6	8.6	10.6	16.0	17.3	17.8
Oxides Recalculated to 100%										
SiO2	75.70	74.99	75.94	76.54	75.78	75.98	75.76	75.10	75.81	75.79
TiO2	0.05	0.00	0.02	0.06	0.03	0.03	0.05	0.00	0.00	0.00
Al2O3	13.64	14.01	13.82	13.14	13.89	13.60	14.06	14.83	14.77	14.96
Fe2O3	0.00	0.00	0.00	0.00	0.00	0.00	0.00	0.00	0.10	0.02
MgO	0.00	0.00	0.02	0.00	0.01	0.00	0.00	0.16	0.14	0.15
CaO	1.30	1.33	1.12	1.04	1.17	1.22	1.46	2.02	1.99	2.07
BaO	0.02	0.00	0.11	0.00	0.06	0.00	0.00	0.00	0.08	0.03
Na2O	3.31	3.30	2.88	2.96	2.96	3.24	3.16	3.83	3.26	3.69
K2O	5.99	6.37	6.08	6.26	6.09	5.93	5.51	4.05	3.85	3.27

C. Compositions of Mordenite in One Fracture

Depth	1315	
SiO2	63.13	61.41
TiO2	0.00	0.00
Al2O3	8.60	9.47
Fe2O3	0.00	0.00
MgO	0.00	0.00
CaO	2.87	2.81
BaO	0.96	0.00
Na2O	1.77	1.98
K2O	0.35	0.44
Total	77.68	76.11
Cation Formulae		
Si	30.95	30.54
Ti	0.00	0.00
Al	4.97	5.55
Fe	0.00	0.00
Mg	0.00	0.00
Ca	1.51	1.50
Ba	0.18	0.00
Na	1.68	1.91
K	0.22	0.28
Coordination of Cations		
Tet.	35.92	36.09
Other	3.59	3.69
Ratio of Si to Al+Fe		
	6.23	5.50
Al+Fe/2Mg+2Ca+2Ba+Na+K		
	0.94	1.07
Mol.% Potassium,Sodium,and Calcium plus Magnesium		
K	6.4	7.6
Na	49.4	51.8
Ca+Mg	44.2	40.6
Oxides Recalculated to 100%		
SiO2	31.27	0.00
TiO2	0.00	0.00
Al2O3	11.07	0.00
Fe2O3	0.00	0.00
MgO	0.00	0.00
CaO	3.69	0.00
BaO	1.24	0.00
Na2O	2.28	0.00
K2O	0.45	0.00

the section on chemical trends should be used only to compare analyses performed by this method. They are not necessarily as accurate as analyses made by other methods.

Imaging and qualitative composition studies were made on an ISI model DS-130 scanning electron microscope, operated between 15 to 40 keV. Qualitative analyses from primary x-ray signals were obtained on a Kevex model 7000 energy-dispersive system with the electron beam operating at 15 keV. Semiquantitative analyses were attempted on open fractures, but the roughness of the sample surface and the absorption of x-rays by the gold coat on the sample made the analyses useful only for mineral identification, not for determining trends in mineral composition with depth. In particular, sodium may have been lost during many analyses. Aluminum values given by standardless qualitative analyses are also lower than the actual values. Although the apparent Si:Al ratios obtained by this method are therefore much higher than the actual ratios, the apparent ratios for known zeolites are distinctive and are much higher than for feldspars. Although clays cannot be distinguished using Si:Al ratios, comparing cations present with zeolite analyses from the drill hole indicates whether the material in question might be a zeolite. The SEM photographs used in this report are of secondary-electron images.

III. Descriptions of Fracture Linings by Stratigraphic Unit

Topopah Spring Member of the Paintbrush Tuff

Lower Lithophysal Zone (770-1128 ft)

Lithophysal-type fractures contain a coarsely interlocking granular lining of silica minerals (quartz, tridymite, and cristobalite) and alkali feldspar. Trace amounts ($\leq$1%) of oxide materials occur on the fracture surfaces and interstitially between quartz grains (Fig. 3). These oxide minerals include bladed crystals (pseudobrookite?), massive interstitial manganese oxides (probably lithiophorite), iron and manganese oxides and intergrowths of varying composition, and minor sulfides (Fig. 4). These fractures are characterized by bleached zones several times thicker than the width of the actual fracture (Fig. 5).

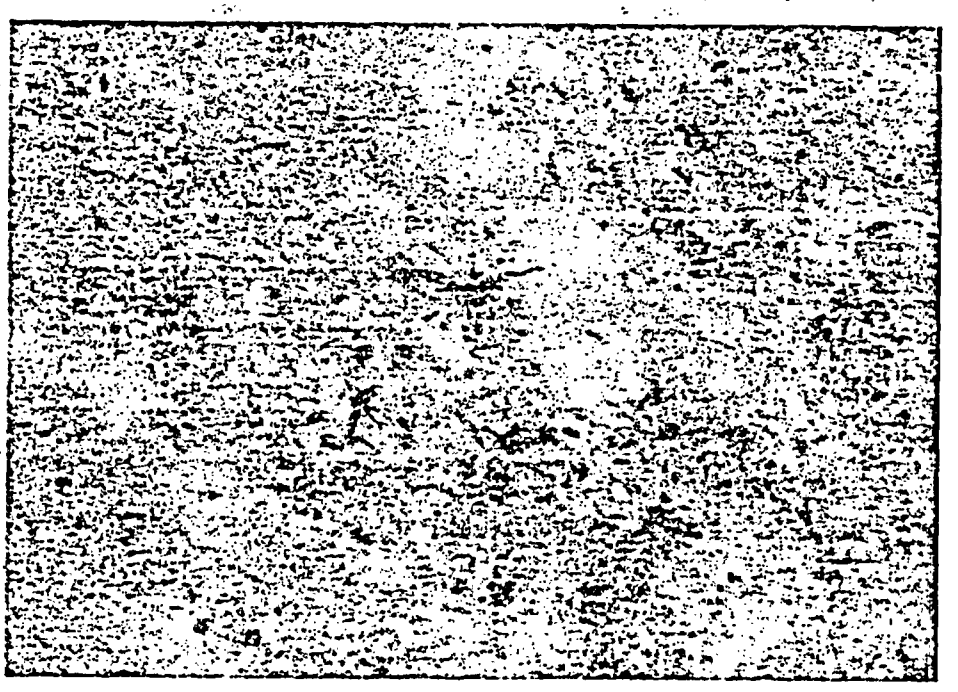

Fig. 3.
Lithophysal-type fracture. Sample is from 984 ft.; field of view is 3 mm.

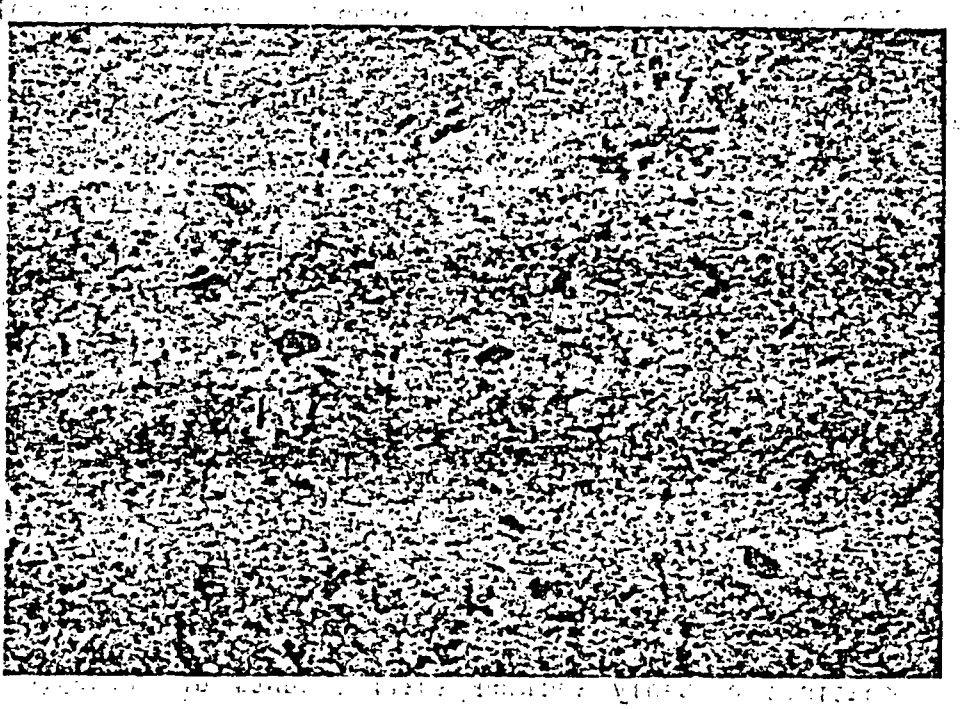

Fig. 4.
Pseudobrookite(?) and manganese and iron oxides on surface of lithophysal-type fracture. Blue-white patches are mordenite. Sample is from 1008 ft; field of view is 1 cm.

The bleached zones resemble zones surrounding lithophysae and frequently the fractures connect or extend from lithophysae. The mineralogy of the fractures is similar to that of the lithophysal coatings. These are the initial fractures and are associated with cooling and devitrification of the ash flow. Lithophysal-type fractures in the core may be open or closed (thicker ones are commonly open), but closed fractures may break open during sampling. Fracture-wall coverage by the granular fillings is 100%.

In the lower lithophysal zone, mordenite occurs in most high-angle (>60° dip) fractures as isolated, raised scaly patches varying from a fraction of a millimeter to a centimeter in diameter. Fractures containing mordenite may cut across sealed lithophysal-type fractures (Fig. 6), or mordenite may coat the surface of lithophysal-type fracture filling material. The mordenite is extremely fine grained, blue white to white, and usually has a waxy luster. At high ($\geq$40 x) magnification the patches commonly appear to be banded (like travertine or agate) (Fig. 7). Crystal faces are not visible at 50 x. All of the observed mordenite occurs in open fractures in the core; the closed fractures sampled in the lower lithophysal zone are all of the lithophysal type. However, mordenite patches coat only 5-15% of the surface of the fractures in which they occur and might not be detectable in closed fractures. The abundance of mordenite within the fractures increases with depth. Some of the fractures that contain patches of mordenite and no lithophysal fill material are partly covered (~1-2%) by raised patches, as large as 1-mm diameter, of manganese oxides of undetermined mineralogy (Fig. 8). Because these manganese-oxide patches are not in direct contact with the mordenite, their paragenetic relationship could not be determined.

Slickensides (usually red brown) are developed on, and therefore postdate, the mordenite and manganese minerals (Fig. 9). In the one fracture in which they were readily detectable at 20 x magnification, the rake of the slickensides was horizontal, nearly parallel to the plane of foliation of the densely welded tuff. Soft, red-stained coatings probably include small amounts of mordenite and a paste of rock fragments. An SEM photograph of mordenite from 810 ft shows slickensides (Fig. 10).

Fig. 5.
Bleached zone surrounding lithophysal-type fracture. Sample is from 1072 ft; field of view is 1.5 cm.

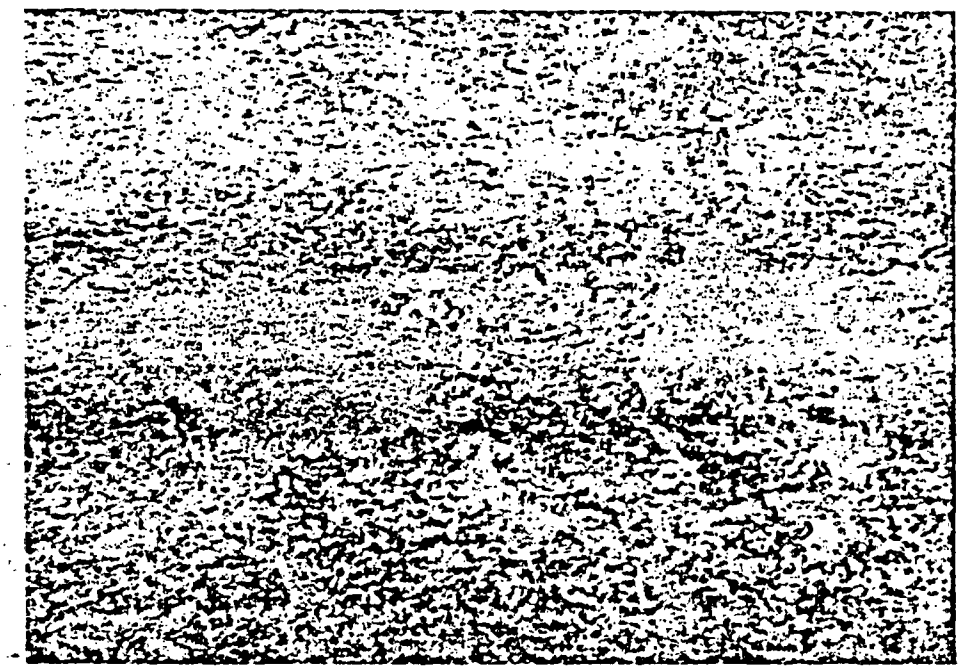

Fig. 6.
Mordenite coating trace of same lithophysal-type fracture shown in Fig. 5. Field of view is 1 cm.

Fig. 7.
Closeup of mordenite patch seen in Fig. 6 showing banding and waxy luster. (Red color is paint used to mark core.) Field of view is 3 mm.

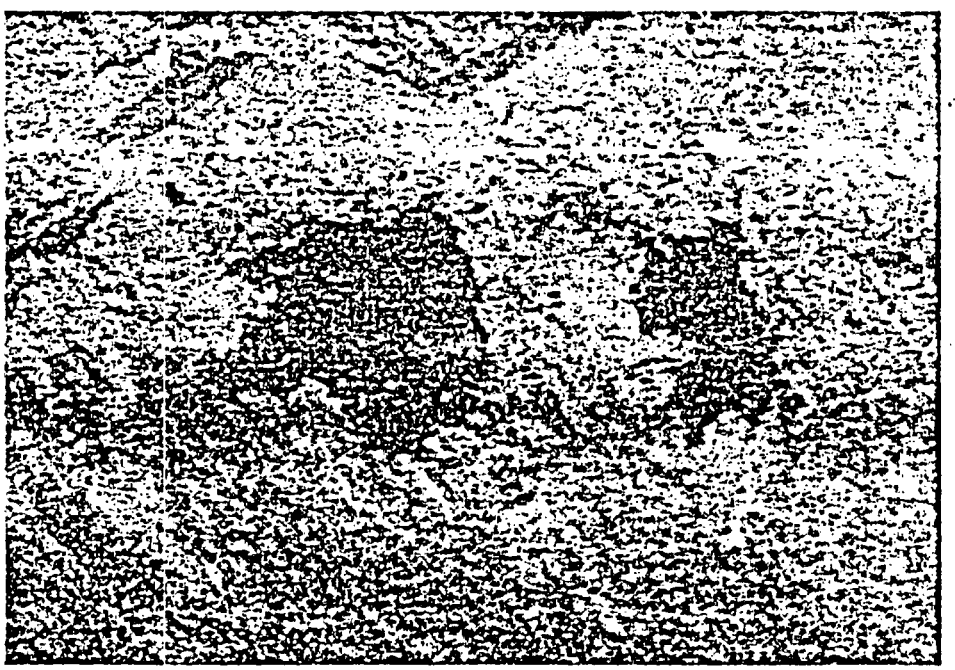

Fig. 8.
Raised patch of manganese mineral(s). White areas are devitrification in host rock. Sample is from 1111 ft; field of view is 5 mm.

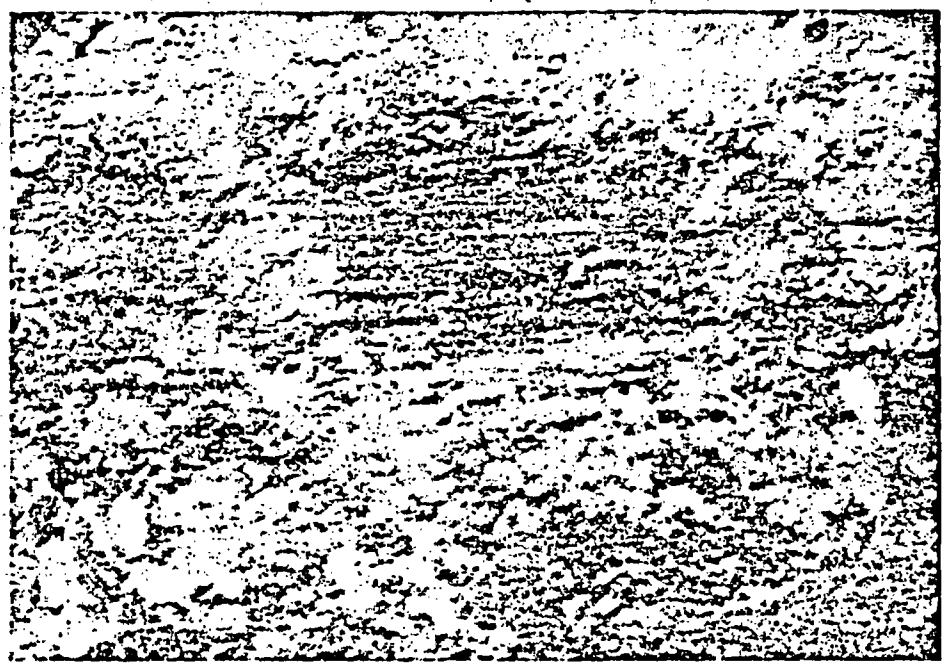

Fig. 9.
Slickensides striating mordenite and manganese minerals at 1084 ft. Field of view is 3 mm.

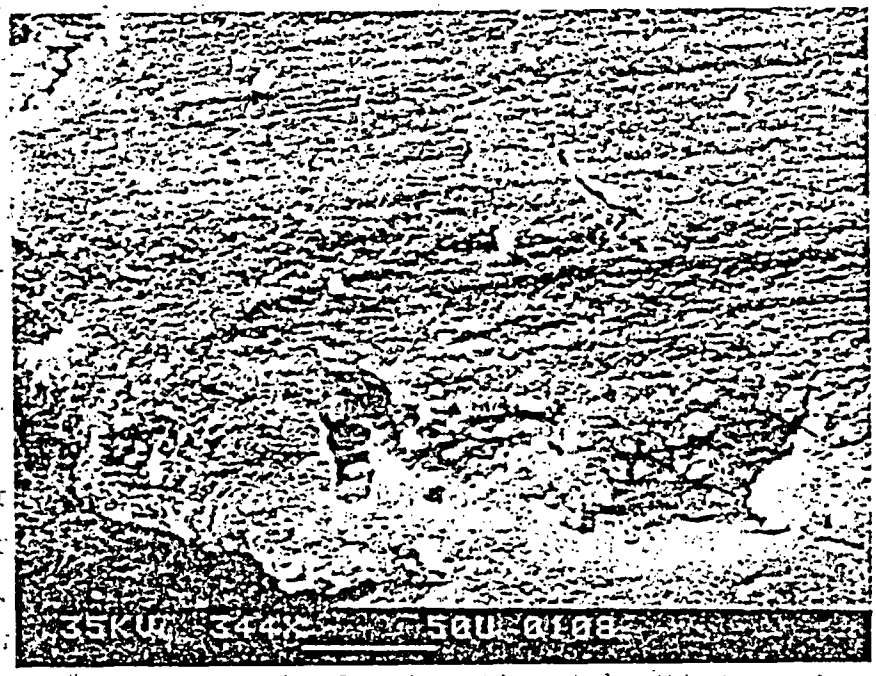

Fig. 10.
SEM image of slickensided mordenite with late clays dotting surface. Sample is from 810 ft.

Slickensides generally predate white powdery coatings of smectite and mineral fragments that constitute the final type of fracture fill observed in this interval. This white or beige, fine-grained material displays no crystal morphology at 50 x magnification. In SEM images some of these coatings have the morphology of smectite (Fig. 11). Qualitative elemental analyses indicate highly variable composition for these powders. Fragments of feldspar and silica minerals incorporated into the coatings probably represent devitrified tuff ground into a powder. Whether these fragments are the result of tectonic movement or drilling cannot be determined. They may have been deposited in open fractures before or during drilling. Euhedral crystals of these minerals were not found (Fig. 12). Some of these coatings form cellular patterns (Figs. 12 and 13). Where the powdery coatings occur with mordenite they coat the surface of the mordenite and thus postdate its deposition. White and beige powders coat from 10 to 90% of the surface of the fractures in which they occur. The powders have only been noted in open fractures; if they occur in closed fractures, the grains may be too small to identify.

A single open fracture lined with calcite 2-3 mm thick on one side was noted in this interval but was not sampled. The calcite vein does not intersect any other fractures in the core and the paragenetic relation of calcite to other fracture minerals is unknown.

Lower Nonlithophysal Zone (Candidate Host Rock) (1128-1316 ft)

Lithophysal-type fractures occur throughout the nonlithophysal zone, although they are less abundant and thinner than in the lithophysal zone and are usually subhorizontal. They are characterized by bleached zones.

A set of near vertical fractures with similar mineralogy occurs in this zone. These fractures contain coarse granular, locally euhedral quartz and feldspar in flattened crystals (Fig. 14). Minor (<1%) cryptocrystalline, massive manganese-oxides occur with the silicate minerals. Unlike the lithophysal-type fractures, these fractures contain no tridymite and lack a surrounding bleached zone. Mordenite partially coats manganese oxides and quartz in one fracture of this

Fig. 11.
SEM image of clay "balls" on fracture surface at 869 ft.

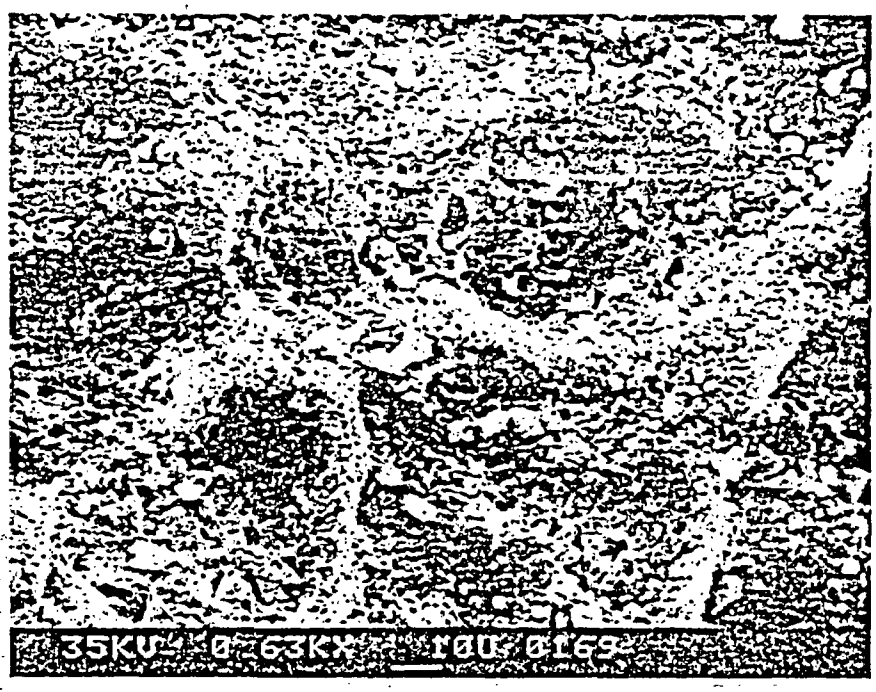

Fig. 12.
SEM image of cellular deposit of silica and feldspar fragments from the same fracture shown in Fig. 11.

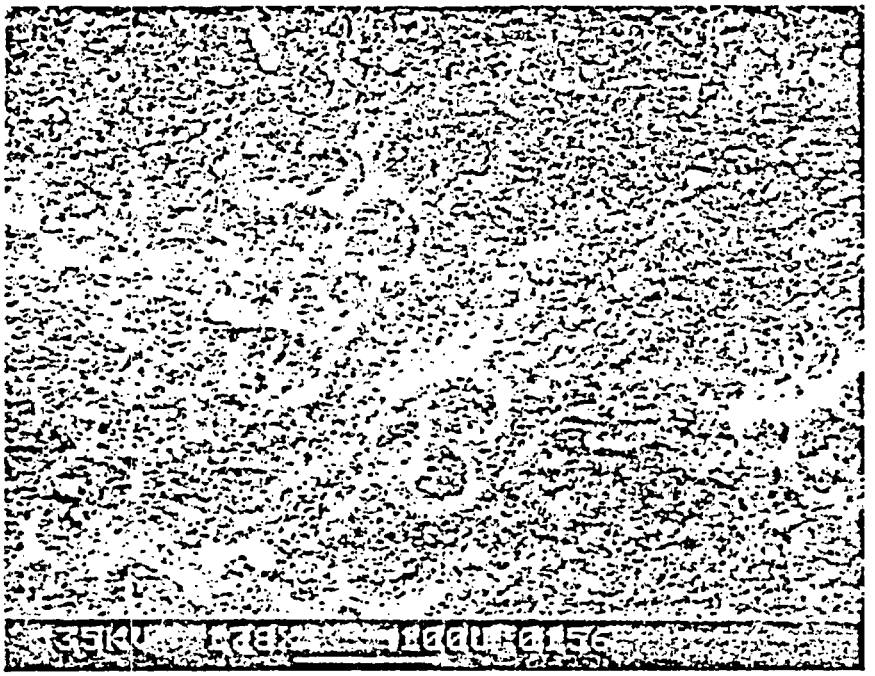

Fig. 13.
SEM image of cellular deposit of fragments and/or clays from same fracture shown in Fig. 12. At this magnification the different types of particles are mostly indistinguishable.

Fig. 14.
Nonlithophysal, flattened quartz and feldspar. Sample is from 1132 ft; field of view is 3 mm.

type (Fig. 15). Fine-grained powder coats the coarse quartz, feldspar, manganese oxides, and mordenite in places and obviously postdates them (Fig. 16). The relationship of these fractures to the lithophysal type was not observed.

Blue-white, cryptocrystalline mordenite coatings in high-angle fractures are increasingly abundant with depth in this interval. The extent of surface coverage by mordenite within the fractures and the size of the fibers seen in SEM images also increase with depth.

Approximately halfway through this interval (first noted at 1245 ft) heulandite occurs in fractures that range from horizontal to vertical. Fractures containing heulandite are usually nearly 100% coated and almost all contain some mordenite. The heulandite occurs as coarse euhedral crystals of either prismatic or tabular morphology (Figs. 16 and 17). The mordenite that occurs with heulandite is coarser than the cryptocrystalline variety found alone in fractures at shallower depths, and in many places it resembles cobwebs draped over the heulandite (Figs. 17 and 18). In some fractures heulandite coats the earlier blue-white cryptocrystalline mordenite (Figs. 19 and 20). Heulandite also coats the manganese and iron oxides in these fractures (Figs. 21 and 22).

Slickensides in high-angle fractures in this interval are stained red and most are nearly horizontal. Slickensides striate the mordenite and manganese minerals (Fig. 23) but not the heulandite. If heulandite coats slickensides, the striations cannot be seen through the zeolite crystals.

As in the overlying lower lithophysal zone, a fine-grained powder of fragments, and possibly smectite, coats the mordenite and the slickensides. SEM photos show what appear to be clay minerals postdating heulandite (Figs. 19 and 24). The mineralogy of these small grains could not be determined by qualitative elemental analyses from the SEM.

A few sparry calcite veins occur near the base of this interval. They are often thick (1-3 mm) and massive and translucent to opaque white. Cristobalite lines the walls of closed fractures in the same interval and mordenite fills the centers. In open fractures calcite postdates the mordenite (Fig. 25). One calcite-filled fracture coats

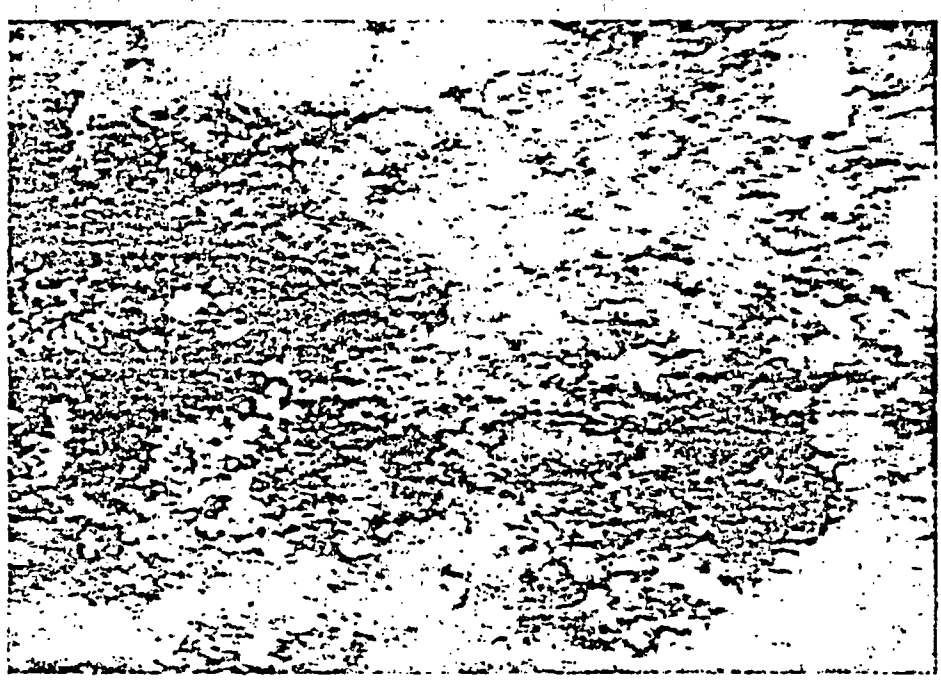

Fig. 15.
Powdery coating on mordenite, manganese minerals, surface of nonlithophysal quartz, and feldspar. Sample is from 1201 ft; field of view is 3 mm.

Fig. 16.
Crystals of heulandite on surface of fracture from 1310 ft. Field of view is 2.5 mm.

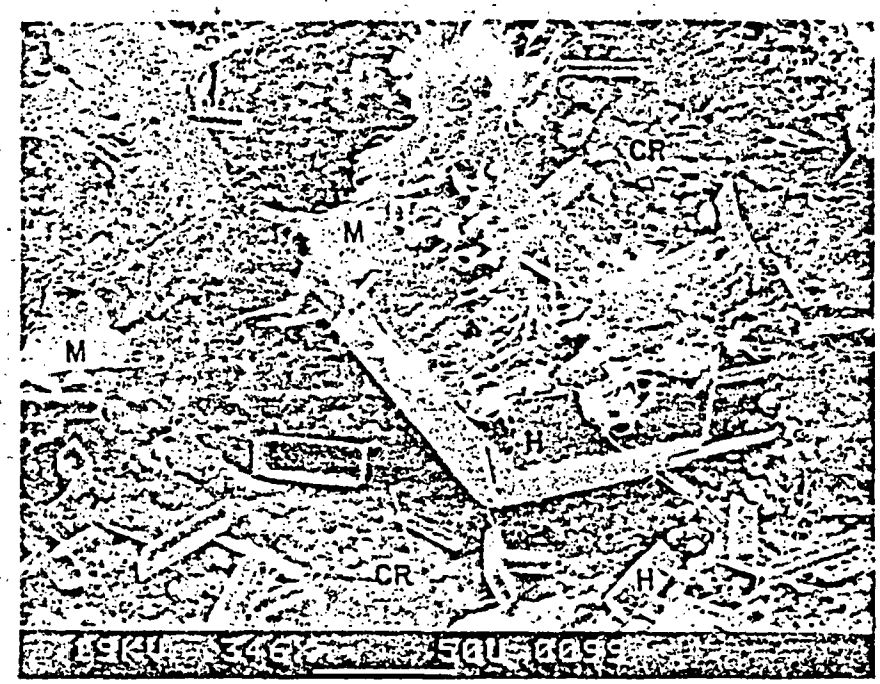

Fig. 17.
SEM image of prismatic and tabular heulandite (H) over cristobalite (CR). Late mordenite (M) drapes heulandite. Fracture is from 1310 ft.

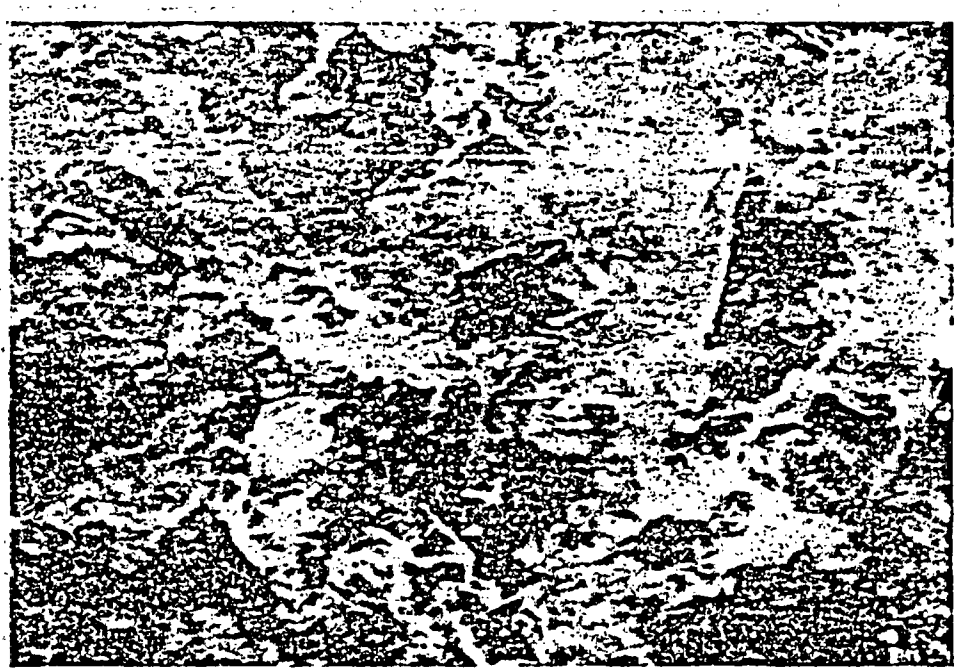

Fig. 18.
Mordenite (blue translucent mineral) draped over heulandite (euhedral crystals) in same fracture shown in Fig. 16. Field of view is 3 mm.

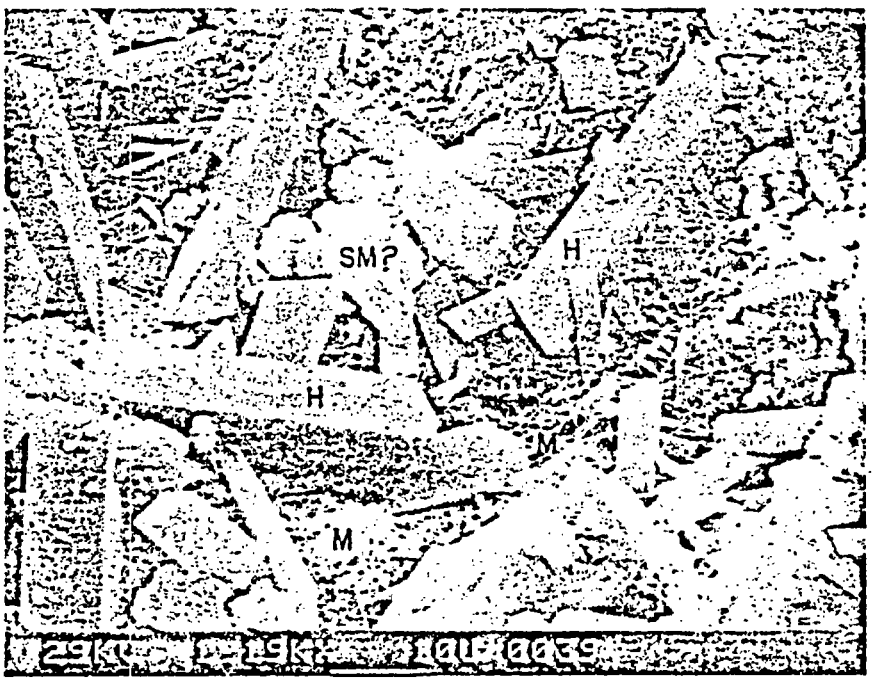

Fig. 19.
SEM image of prismatic heulandite (H) over mordenite (M). Late clays (SM?) on heulandite. Sample is from 1254 ft.

Fig. 20.
Tabular heulandite over mordenite on surface of fracture from 1310 ft. Field of view is 2.5 mm.

Fig. 21.
Clear heulandite coating iron and manganese oxides on surface of fracture from 1258 ft. Field of view is 2.5 mm.

Fig. 22.
SEM image of heulandite coating iron mineral, possibly hematite. Sample is from 1258 ft.

Fig. 23.
Slickensides at 1244 ft striating mordenite and manganese mineral. Field of view is 3 mm.

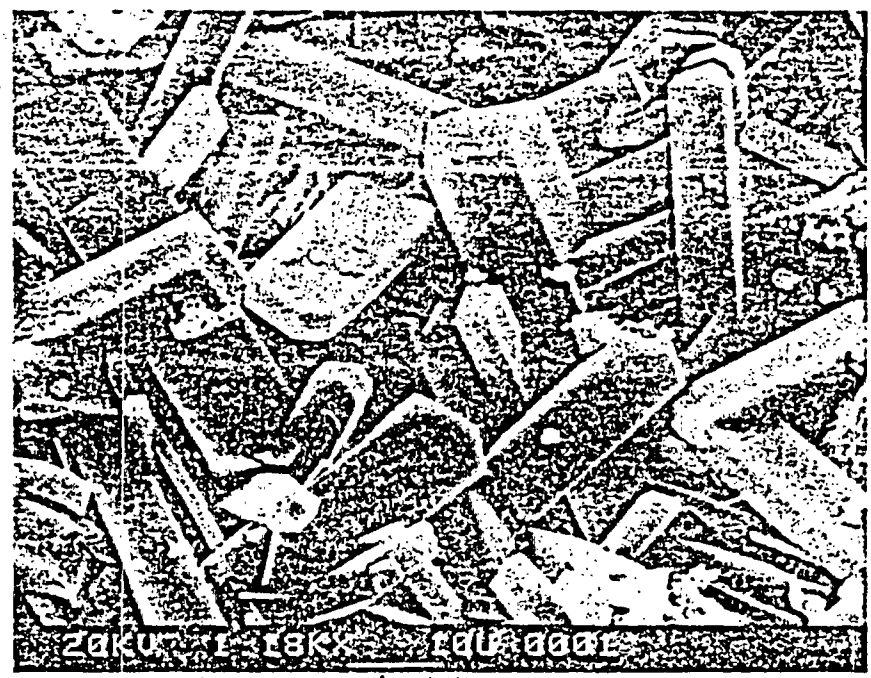

Fig. 24.
SEM image of heulandite coating fracture surface at 1258 ft. Small light crystals are late clays.

the trace of an earlier mordenite-filled fracture of different orientation. Cristobalite, if present, is not identifiable at 50x magnification. The calcite is not slickensided, but does exhibit well-developed cleavage that might result from strain.

Vitrophyre and Underlying Nonwelded Vitric Zones (1316-1378 ft)

Textures of the fracture minerals in this interval differ considerably from those in the devitrified zone above. Megascopic and identifiable microscopic crystals are nonexistent; instead, the fracture fill is cryptocrystalline and is identified by XRD as primarily heulandite and mordenite. Smectite is more abundant (based on XRD data) than in higher intervals but, like the other cryptocrystalline minerals, it cannot be identified optically even at 50x.

The vitrophyre contains abundant vertical and nearly vertical fractures (as closely spaced as 1-2 mm in the lower part). Sparse, subhorizontal fractures predominate near the middle of the interval. All fractures are coated with as many as three layers of submicrometer grained, pasty material. A thin blue layer, primarily heulandite, and cristobalite, lines all vertical fractures. It is postdated by a cream-colored coating up to 1 mm thick of smectite and heulandite (Fig. 26). The widest fractures have a final coat of beige material that is primarily heulandite and mordenite. The layers are identifiable by color and can be flaked off and separated fairly readily. Mineral identifications are based on XRD analyses because individual crystals are not optically identifiable even at 2000x. Because smectite apparently does not form a separate layer it must be intergrown with the zeolites. Slickensides indicate that movement along many of these fractures occurred after the coatings were deposited (Fig. 26). Subhorizontal fractures were not examined.

The underlying nonwelded vitric zone (1345-1378 ft) has few vertical or high-angle fractures. Fracture coatings are sparse and are discontinuous where they occur. In the upper part of the interval, where they are thickest, the coatings megascopically resemble coatings in the vitrophyre. Deeper in the vitric interval, coatings are sparser and appear powdery. Microscopically, all of the coatings consist of

Fig. 25.
Calcite (white mineral) lining fracture previously coated with mordenite and possibly cristobalite from 1315 ft. Field of view is 1 cm.

Fig. 26.
Submicrometer cryptocrystalline coatings from fracture at 1341 ft. Blue and cream-colored layers are shown. Striations in the cream-colored layer are slickensides. Field of view is 3 mm.

balls or clusters (up to 0.5 mm diameter) of white to clear, 0.01–0.02-mm crystals (Fig. 27). Three SEM samples show a mineral with the morphology of smectite (Fig. 28), but the XRD data indicate primarily heulandite with only minor smectite in the two samples analyzed. Mordenite, which was identified by XRD in the sample at 1362 ft, was visible only by SEM and then as single fibers. Manganese oxides are relatively abundant in the upper part of the interval (coating up to 40% of the fracture surface) and apparently occur between the host rock and the white coating. Both the manganese oxides and the white coating are striated by slickensides (Fig. 29).

Nonwelded Zeolitic Base of Topopah Spring Member of the Paintbrush Tuff and Underlying Bedded Unit (1378–1409 ft)

Fractures are not common in the nonwelded zeolitic interval at the base of the Topopah Spring Member, but the few present are continuous over several feet although not all are filled. The samples studied are from a lithic-rich zone (1378 to 1388 ft) but appear to represent the entire interval. An open fracture at 1381 ft has a clearly crystallized coating; the blocky crystals and individual faces are apparent at 50x and can be seen more clearly in the SEM images at $\geq$100x (Fig. 30). Analysis by XRD indicates that the fracture coating is clinoptilolite and cristobalite. A thin section of the sample from 1381 ft shows younger open veins coated with clinoptilolite crosscutting closed cristobalite veins (Fig. 31). This is the shallowest fracture occurrence of clinoptilolite sampled in USW G-4. The present open fracture did not completely follow the trace of the older clinoptilolite-coated fracture. Apparently clinoptilolite coated 100% of the older fracture, which was wholly or partly sealed and later reopened (during coring?). Portions of the open fracture that do not follow the older fracture contain no coating material.

The sample at 1384 ft has a finer-grained coating of tiny, clear crystals over a smooth botryoidal, translucent surface. The fracture at 1384 ft apparently reopened along an older, partly sealed fracture coated with cristobalite and clinoptilolite. SEM examination shows that the clear crystals are similar to the clinoptilolite in the

Fig. 27.
Clusters of clear to white microcrystalline heulandite on surface of fracture at 1350 ft. Field of view is .3 mm.

Fig. 28.
SEM image of heulandite(?) at 1362 ft. See text.

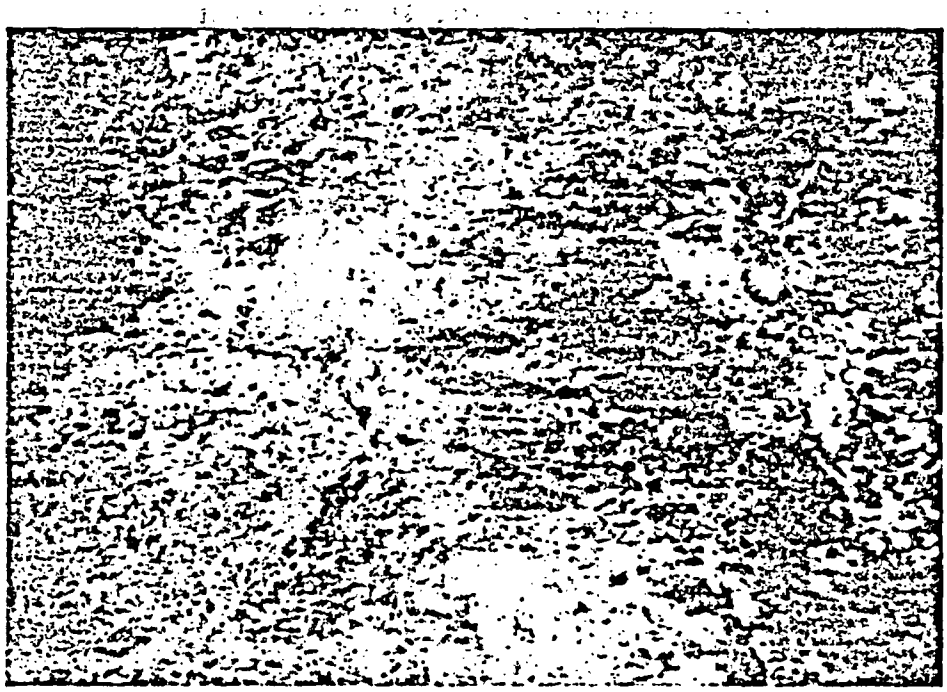

Fig. 29.
Slickensides striating mordenite and manganese minerals at 1350 ft. Field of view is 1 cm.

Fig. 30.
SEM image of clinoptilolite at 1381 ft.

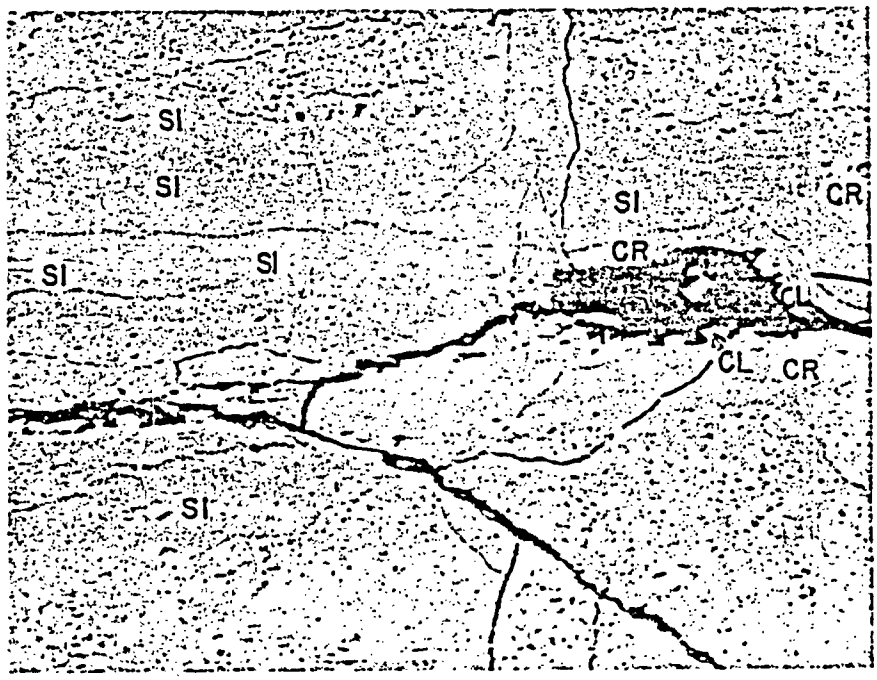

Fig. 31.
SEM image of closed veins filled with silica (SI) (cristobalite?) cut by open veins lined with cristobalite (CR) and clinoptilolite (CL). Sample is from 1381 ft.

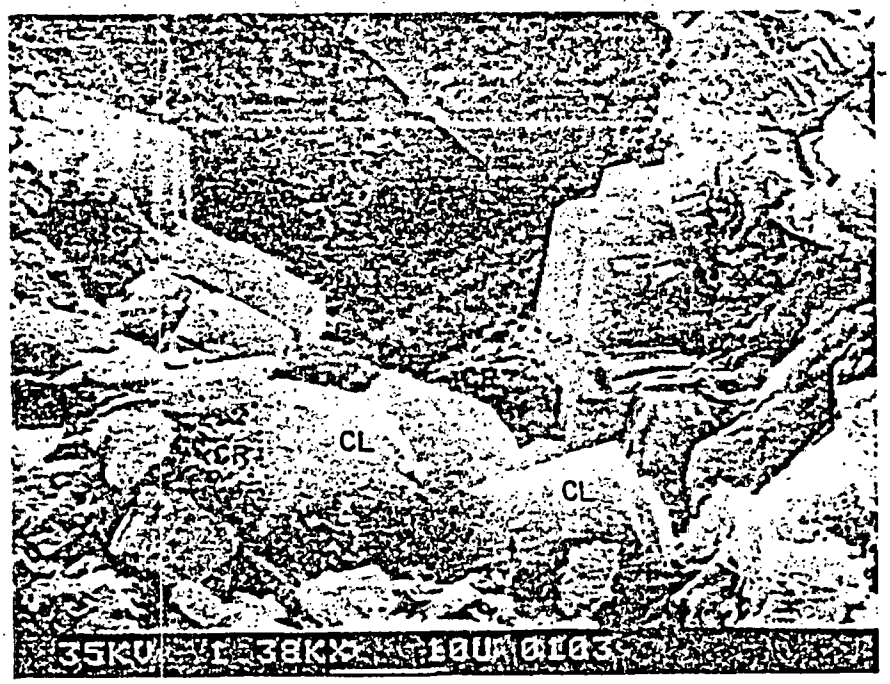

Fig. 32.
SEM image of clinoptilolite (CL) and β-cristobalite (CR) at 1384 ft.

1381-ft sample but have different terminations (compare Fig. 30 with Fig. 32). The surface, which at 50x appeared smooth and botryoidal, is very fine-grained cristobalite.

Tuffs of Calico Hills

Bedded and Nonwelded Tuffs (1409-1705 ft)

Few high-angle fractures occur from 1409 to 1600 ft, but below 1600 ft fractures are slightly more abundant. The coatings of two high-angle fractures at 1436 ft closely resemble those in the lithic-rich zone of the lower nonwelded Topopah Spring Member described above. One of these fractures contains nearly pure microcrystalline clinoptilolite with a dusting of white powder (Fig. 33); the other fracture contains a trace of a similar looking white powder of unidentified mineralogy. The clinoptilolite-lined fracture was the only one observed in this core interval that was coated with microcrystalline crystals (visible at $\leq$50x magnification).

Some fractures in this zone have no coatings and may have been produced during coring or handling. Most coated fractures throughout this interval contain cryptocrystalline material that has a plastery appearance with no visible crystals at 50x magnification (Fig. 34). Dull black stainings and specks, presumably manganese oxides, occur on some coatings, and some are scored with slickensides with rakes of 55-65°.* Analyses by XRD show that these coatings are clinoptilolite, mordenite, and possibly minor smectite. The grains are not microscopically identifiable but can be seen at magnification >1000x on SEM images (Fig. 35 and 36). In addition to euhedral clinoptilolite, which is easily identifiable by its morphology (Fig. 35), many fractures in this interval contain unidentified blocky grains ($\leq$10-cm diameter) embedded in the mordenite mats (Fig. 36). A few fractures have a partial coating (30-40% of the surface) of a white cellular network that, at low magnification, appears similar to that found in the lower lithophysal and lower welded zones of the Topopah Spring Member of the

*Information provided by M. P. Chornack, US Geological Survey (1984).

Fig. 33.
Microcrystalline clinoptilolite in fracture at 1436 ft. Field of view is 5 mm.

Fig. 34.
Cryptocrystalline fracture coating at 1542 ft depth. This is typical of coatings throughout Tuffs of Calico Hills. Field of view is 1 cm.

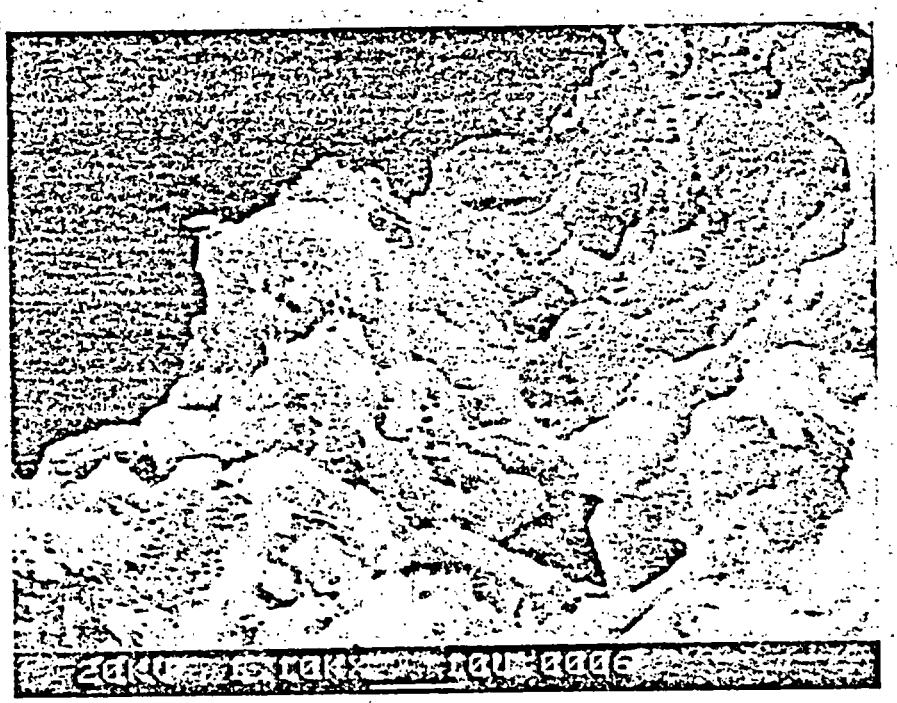

Fig. 35.
SEM image of clinoptilolite draped with mordenite on fracture surface from 1542 ft.

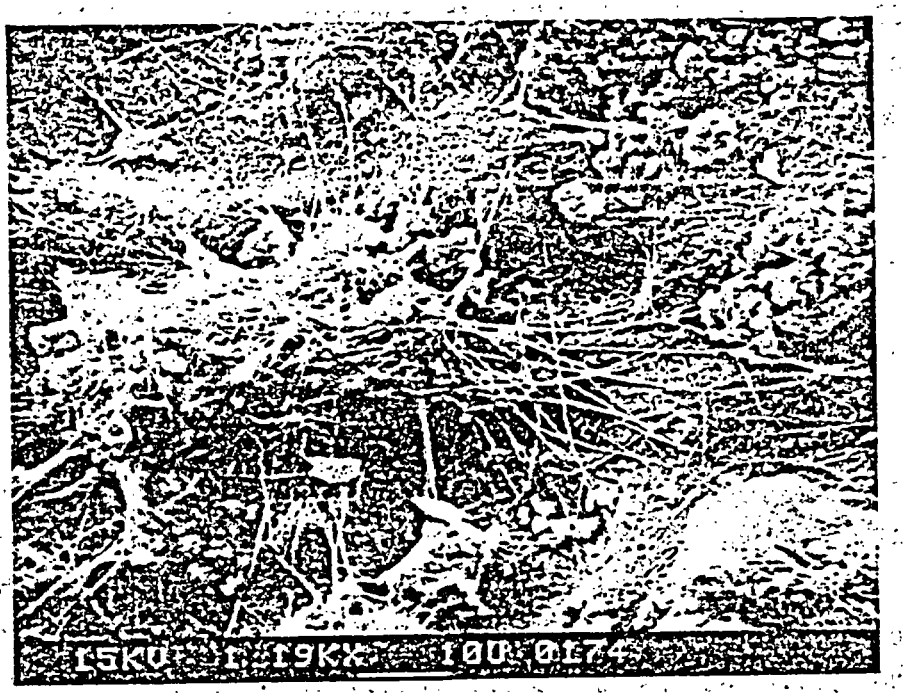

Fig. 36.
SEM image of unidentified blocky grains in net of mordenite that coats fracture from 1569 ft.

Paintbrush Tuff. However, SEM studies of the Tuffs of Calico Hills suggest that these network coatings are mordenite (Figs. 37 and 38) rather than smectite or crushed tuff fragments as seen in the Topopah Spring Member of the Paintbrush Tuff.

Bedded Zeolitic Tuff at the Base of the Tuffs of Calico Hills (1705–1761 ft)

This bedded tuff unit contains fewer high-angle fractures than the nonwelded Tuffs of Calico Hills above it. Horizontal fractures predominate, but there are not many of these. A few fractures contain white or pink coatings, but most have no coatings and may have formed during coring or handling. Where minerals in high-angle fractures are discernible from the zeolitized wall rock, they form a thin gray-white cryptocrystalline (<0.01 mm grain size) coating that covers 20–40% of the fracture surface. Analyses by XRD indicate that the white cryptocrystalline material is mordenite with some clinoptilolite. Orange staining is common but cannot be attributed to any visible mineral. Where both orange and white coatings occur together, the white cryptocrystalline material overlies the stained fracture surface (Fig. 39). A sample at 1721 ft contains small patches of bright-yellow cryptocrystalline chloride(s) (Fig. 40) but the lack of sufficient material prevented XRD analysis; element identification by SEM indicated K, Ti, and some Fe in the chloride.

Prow Pass Member of Crater Flat Tuff

Nonwelded zeolitic tuff [1761–1770 ft (SWL)]

The upper part of this zone contains healed, nearly vertical fractures filled with microcrystalline, clear clinoptilolite (Fig. 41). These thin, healed fractures are difficult to see on the core surface and were identified only because one sample broke open along one of the fractures during the preparation of a sample for SEM study. No continuations of these fractures were identified in the unbroken core disks. The healed fractures are cut by later closely spaced horizontal (disk) fractures that are filled with microcrystalline,

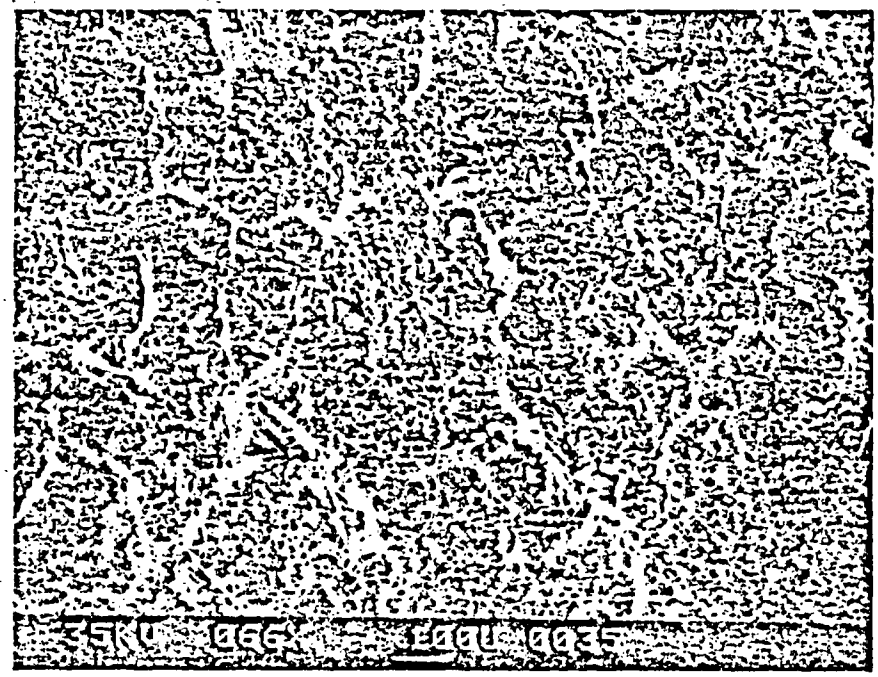

Fig. 37.
SEM image of cellular network of mordenite coating fracture at 1566 ft.

Fig. 38.
Enlargement of network shown in Fig. 37.

Fig. 39.
Gray-white cryptocrystalline coating on fracture at 1707 ft. Field of view is 1 cm.

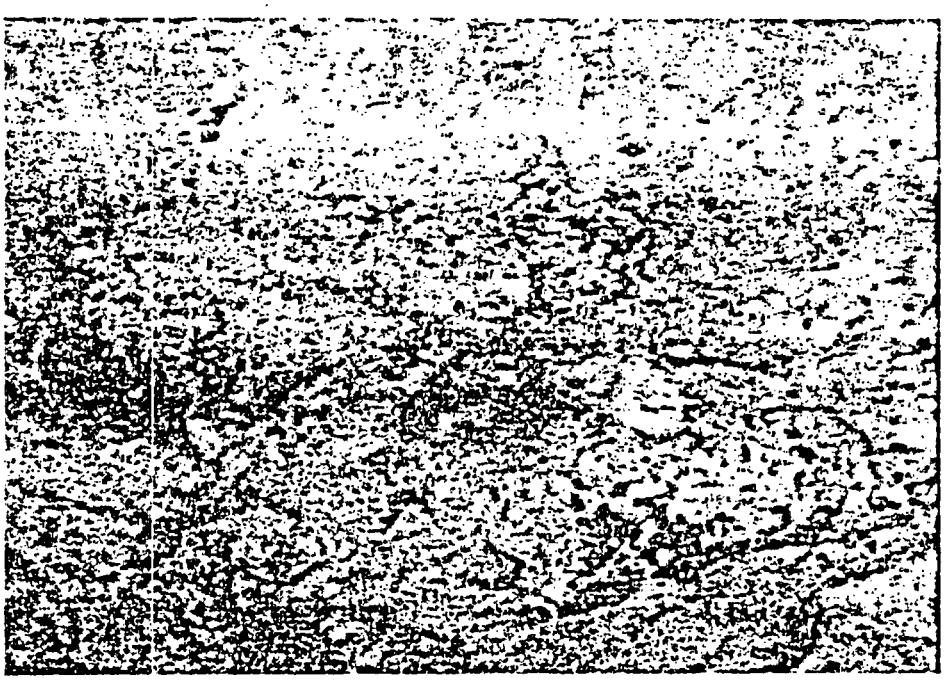

Fig. 40.
Yellow chloride on surface of fracture at 1721 ft. Field of view is 5 mm.

crumbly orange material. This material was determined by XRD to be smectite, possibly with clinoptilolite, that is locally coated with white, waxy cryptocrystalline mordenite (Fig. 42).

Below this upper interval of closely spaced horizontal fractures, vertical and high-angle fractures contain discontinuous, white cryptocrystalline and orange crumbly coatings apparently similar to those noted in the horizontal fractures. Distinguishing these coatings from the zeolitized wall rock, which also contains cristobalite and smectite* is difficult.

IV. Mineralogical and Chemical Trends of Fracture Coatings with Depth

Cryptocrystalline mordenite is the first zeolite that appears in fractures of drill hole USW G-4. It occurs in small amounts at 810 ft at the top of the lower lithophysal zone; it may also occur in fractures at shallower depth. Deeper in the hole, mordenite apparently formed before heulandite. A coarser mordenite crystallized with or after the heulandite. The mordenite at 1315 ft fills closed fractures that are lined with earlier cristobalite. Results of microprobe analyses of the mordenite are given in Table II. Most zeolite-lined fractures in the densely welded zone of the Topopah Spring Member of the Paintbrush Tuff are open, and thin sections across them could not be made. The first zeolite (both in terms of depth and time) to have formed in the fractures is mordenite, whereas the shallowest occurrence of zeolite in the whole rock is heulandite identified from the XRD pattern of core from 1299 ft.*

Apparently two generations of heulandite occur in fractures in the lower nonlithophysal zone. Large tabular crystals ($\leq$0.5-mm diameter) occur on or protrude from the surface coated with much finer grained, more prismatic crystals, whose form can be seen only by SEM. The composition of cryptocrystalline ($\leq$0.005-mm) fracture linings and that of the visible ($\geq$0.02-mm) embedded crystals is identical. The very large euhedral crystals ($\geq$0.2 mm) have not been analyzed.

Heulandite in the vitrophyre has a different habit from heulandite in fractures in the devitrified tuff above it. The XRD pattern still clearly

*Information provided by D. Bish, Los Alamos National Laboratory (1984).

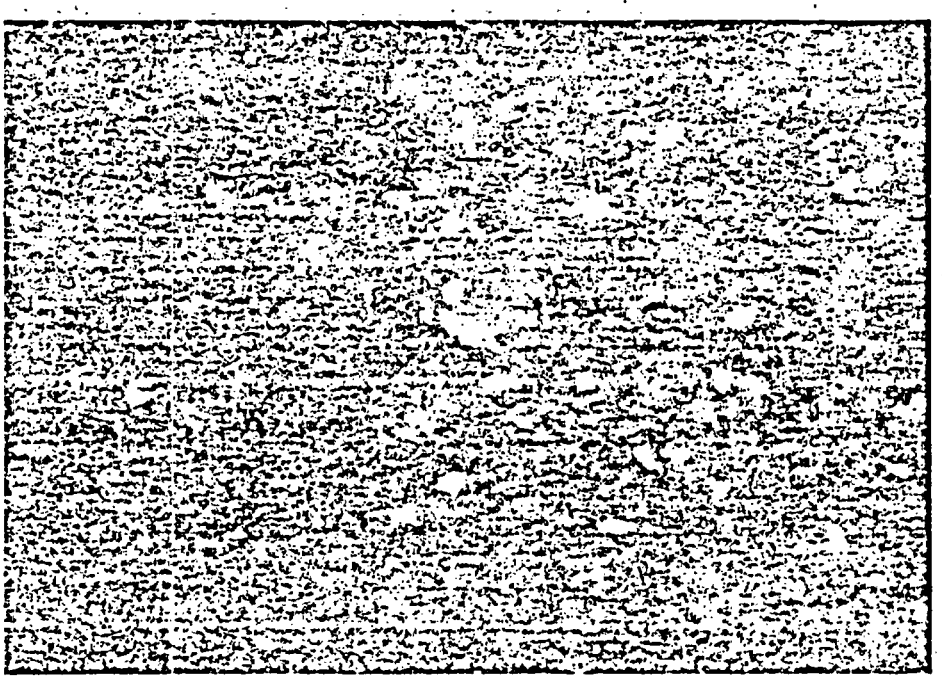

Fig. 41.
Microcrystalline, clear clinoptilolite that lines vertical fractures at 1763 ft. Field of view is 3 mm.

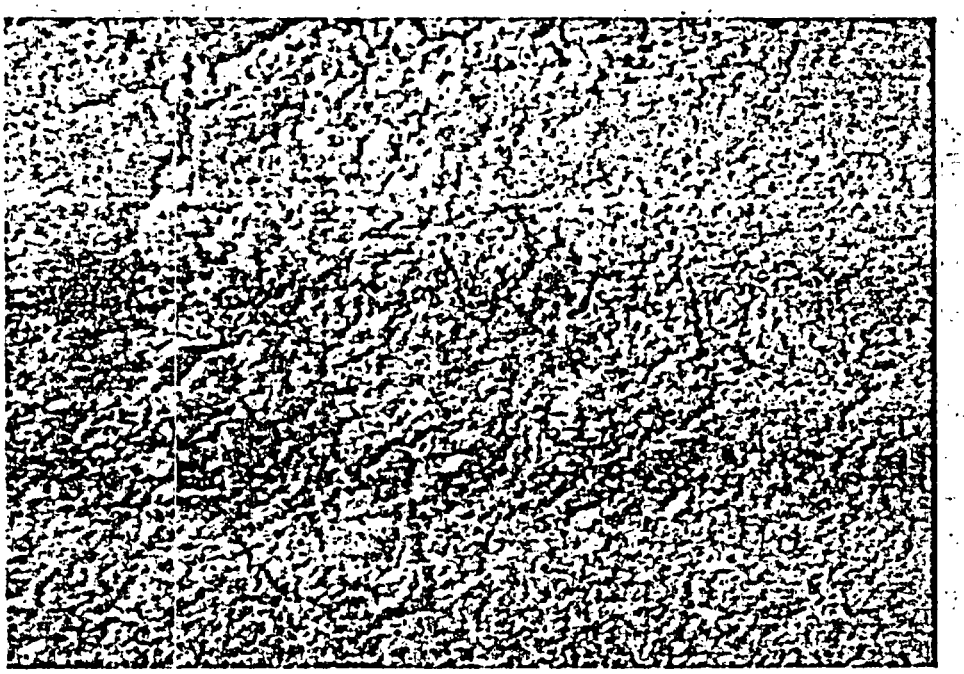

Fig. 42.
Crumbly orange material (smectite and clinoptilolite) coated by waxy white mordenite in horizontal (disk) fractures that cut vertical fractures at 1763 ft. Field of view is 1 cm.

indicates heulandite (rather than an amorphous material), but the peaks are broad rather than sharp (Fig. 43). The material is poorly crystallized, and even at 2000x (SEM) individual crystals are not visible. Microprobe analyses indicate a variable composition, but one that is more sodic and potassic than heulandite at the base of the densely welded zone immediately above (Fig. 44A). Because the XRD peaks are broad and difficult to interpret, and individual crystals cannot be identified in this material, the analyses possibly represent a fine-grained intergrowth of heulandite and some other material rather than pure heulandite. The sample at 1341 ft (from the vitrophyre) is the only heulandite-clinoptilolite that completely decomposed upon heating (Fig. 43). Heulandite from the densely welded devitrified zone above and the vitric zone below had much less intense XRD peaks after they were heated, but the peaks did not disappear completely (Figs. 45 and 46). Partial destruction of heulandite at 450°C was described by Boles (1972). He called these samples Group 2 heulandites and correlated the response to heating with the Si:Al ratio. He defined Group 2 heulandites as having Si:Al ratios $\geq$3.57, whereas Group 1 heulandites, which are destroyed by heating to 450°C for 15 hours, has Si:Al ratios $\leq$3.52. Few analyses have been performed on heulandite from fractures in USW G-4, but most have Si:Al ratios $\geq$3.7 (Fig. 47).

Smectite clays first appear in abundance in the vitrophyre. XRD analysis of a glycolated, sedimented sample indicated nonordered interstratified dioctahedral smectite/illite with $\geq$75% smectite. The small sample size gave poorly defined peaks that prevented more precise interpretation.

Heulandite in the vitric tuff underlying the vitrophyre is microcrystalline, visually unidentifiable at 50x magnification, but visibly crystallized. SEM photos show nothing that resembles the familiar forms of heulandite (compare Fig. 22 with Fig. 27). The XRD analysis of the sample from 1350 ft has a clear heulandite pattern with only about 10% smectite (Fig. 46). Heulandite and minor smectite are also indicated in the sample from 1362 ft, although its pattern is obscured by a background of vitric material. After both samples were heated, XRD patterns indicated heulandite rather than clinoptilolite. No closed fractures were found for thin-section analysis in these samples.

Fracture coatings within the entire glassy section (vitrophyre and nonwelded vitric tuff below it) are quite different from coatings within the

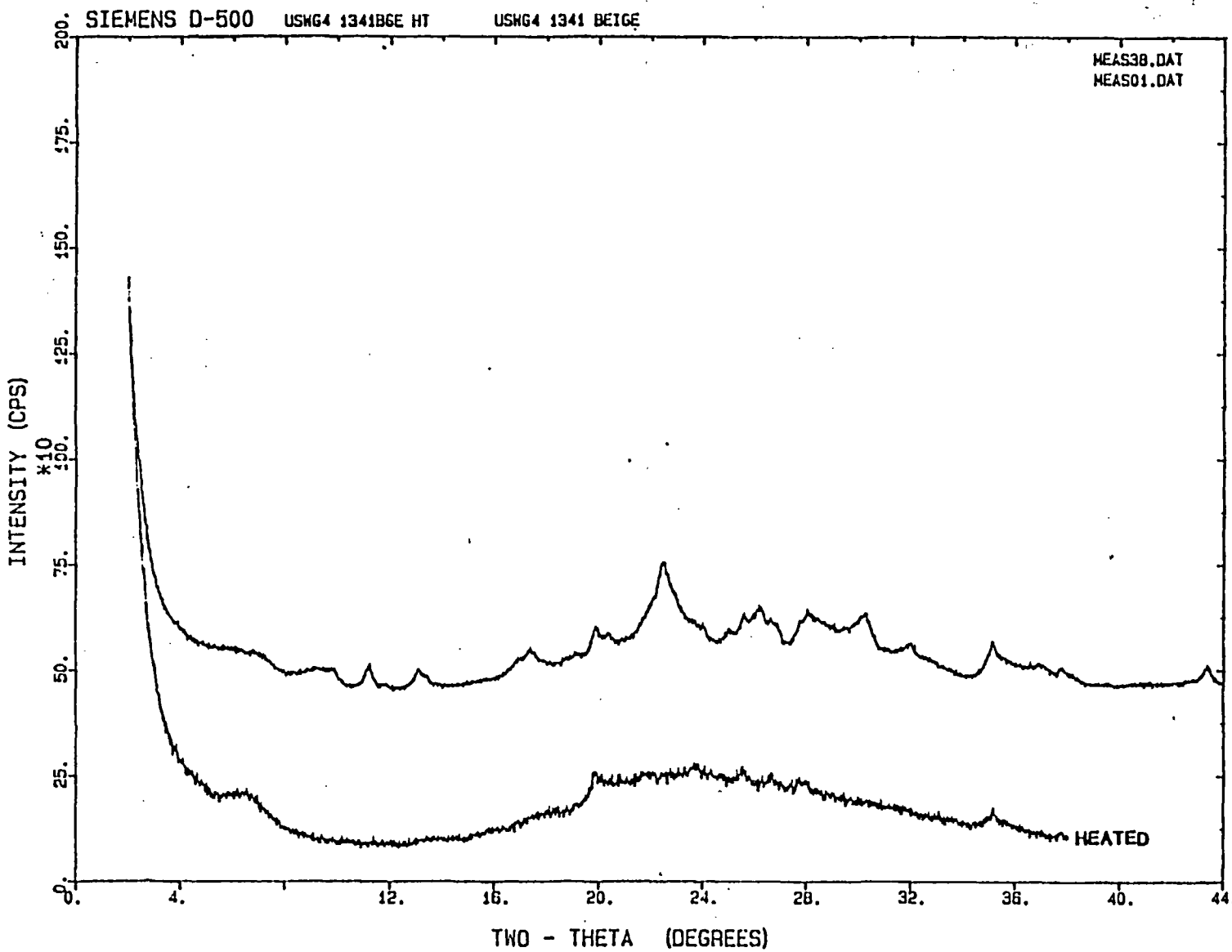

Fig. 43.

XRD pattern of sample from 1341 ft showing broad peaks before heating and pattern after being heated to 450°C overnight.

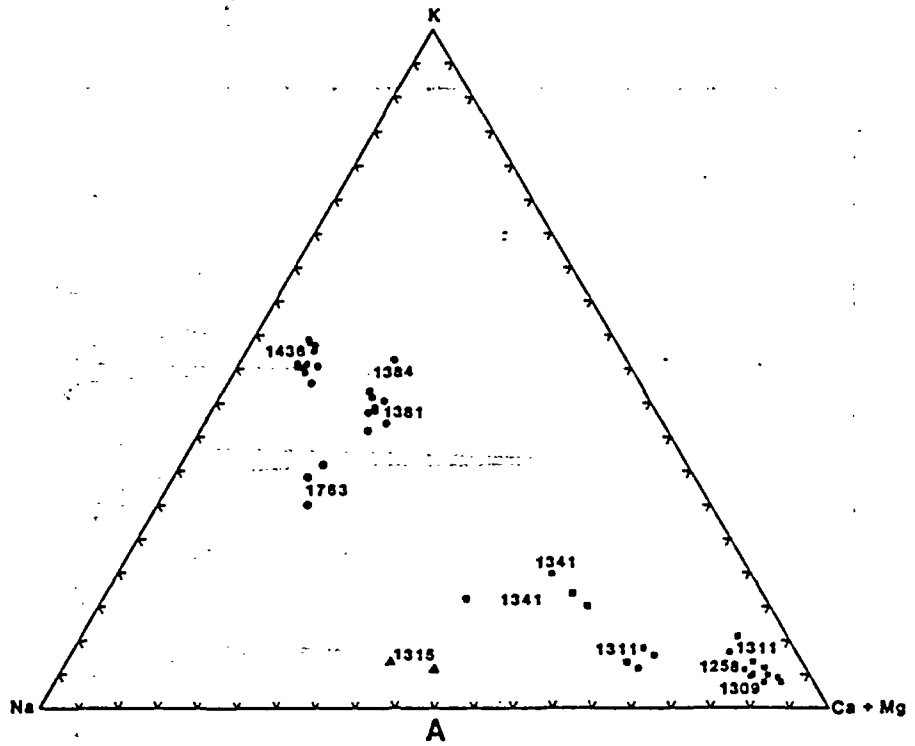

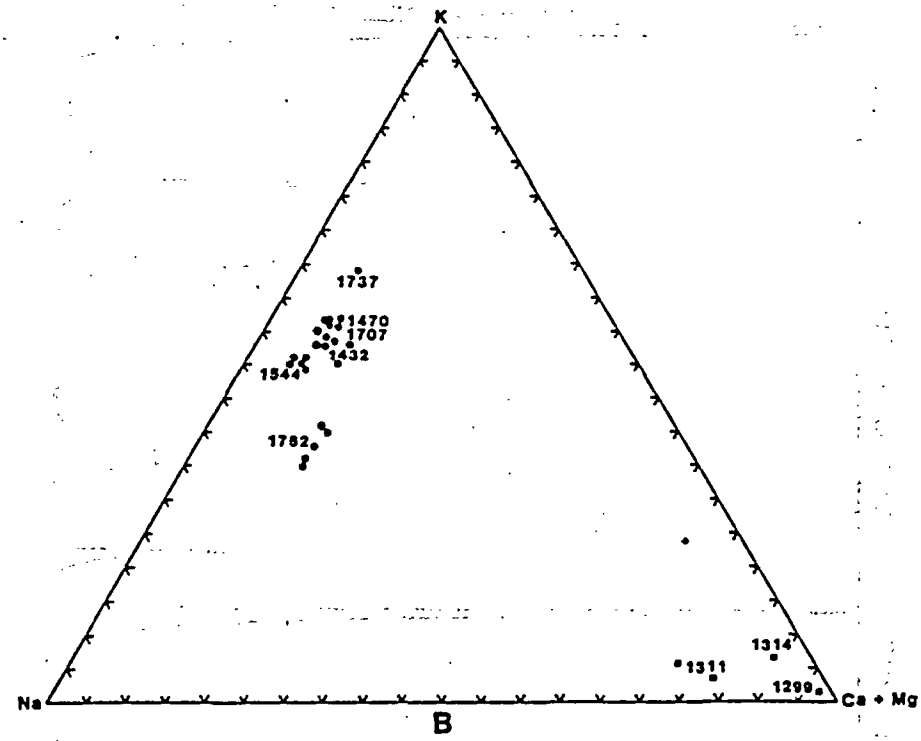

Fig. 44.
Na-K-Ca+Mg ternary plot of zeolites in the unsaturated zone of USW G-4. A - Fracture lining minerals; B - host rock. Clinoptilolite data in B from D. Broxton, Los Alamos National Laboratory, 1984, heulandite data in B from S. Levy, Los Alamos National Laboratory, 1984.

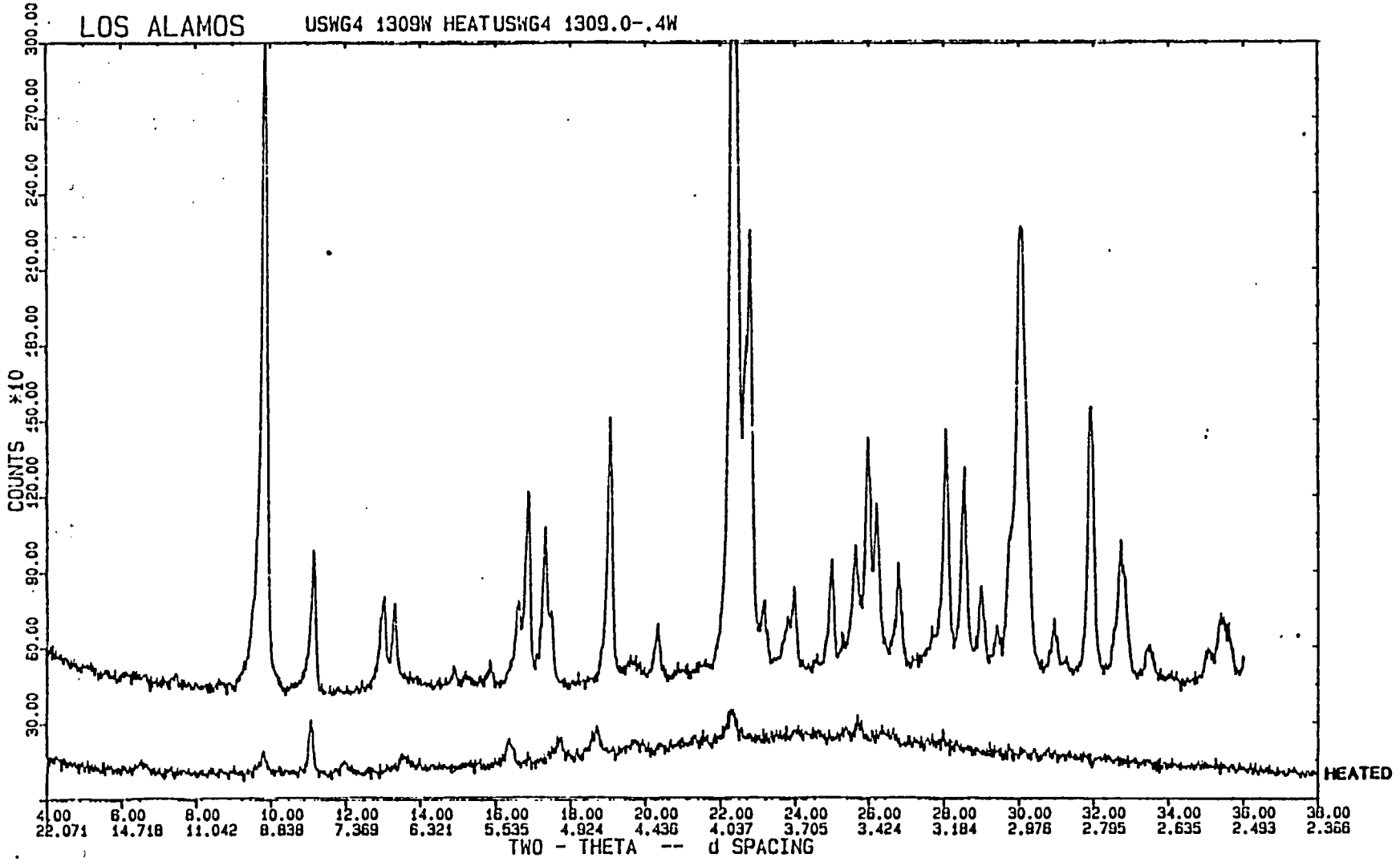

Fig. 45.
XRD patterns of sample from 1309 ft before and after heating.

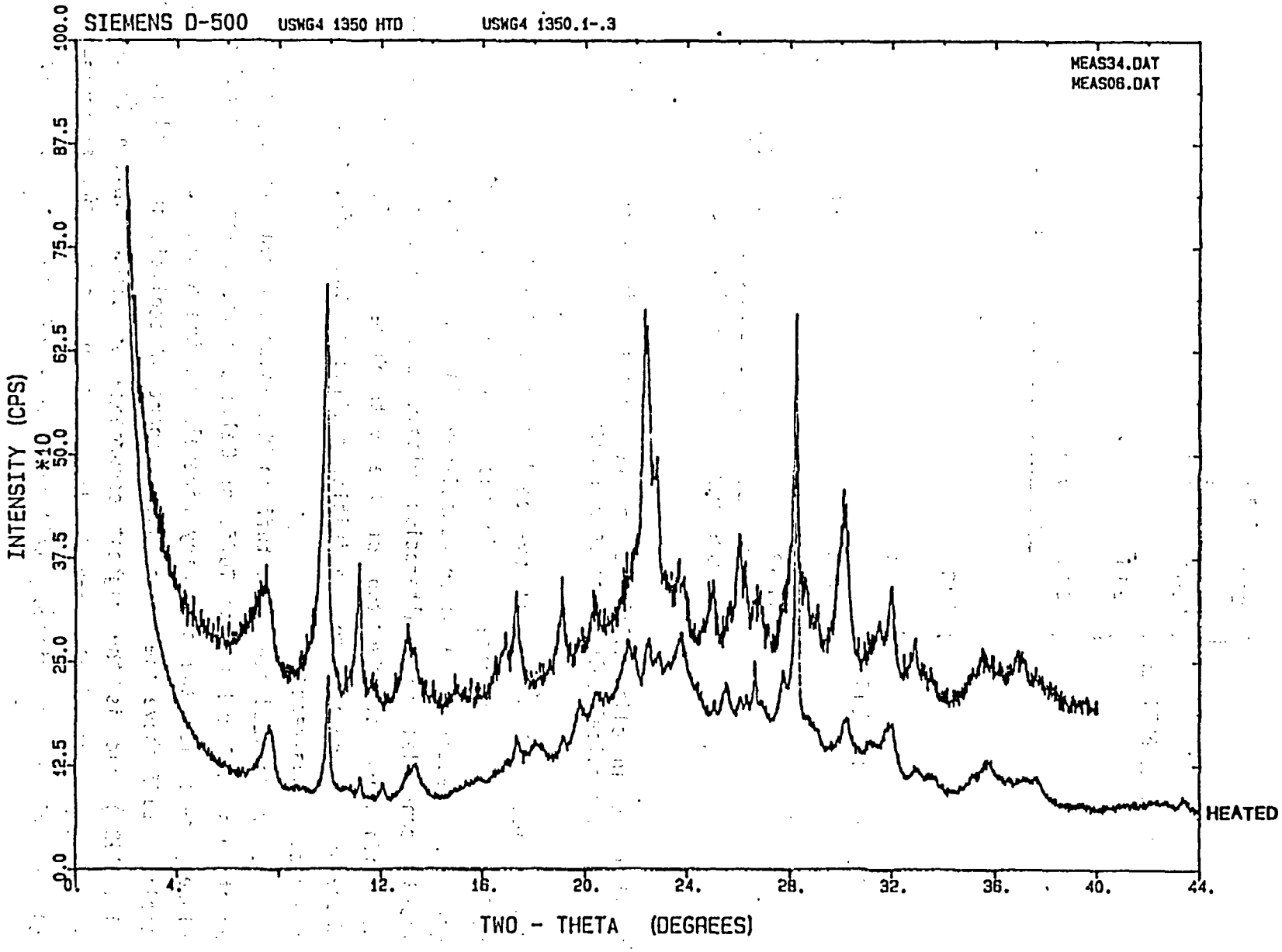

Fig. 46.
XRD patterns of sample from 1350 ft before and after heating.

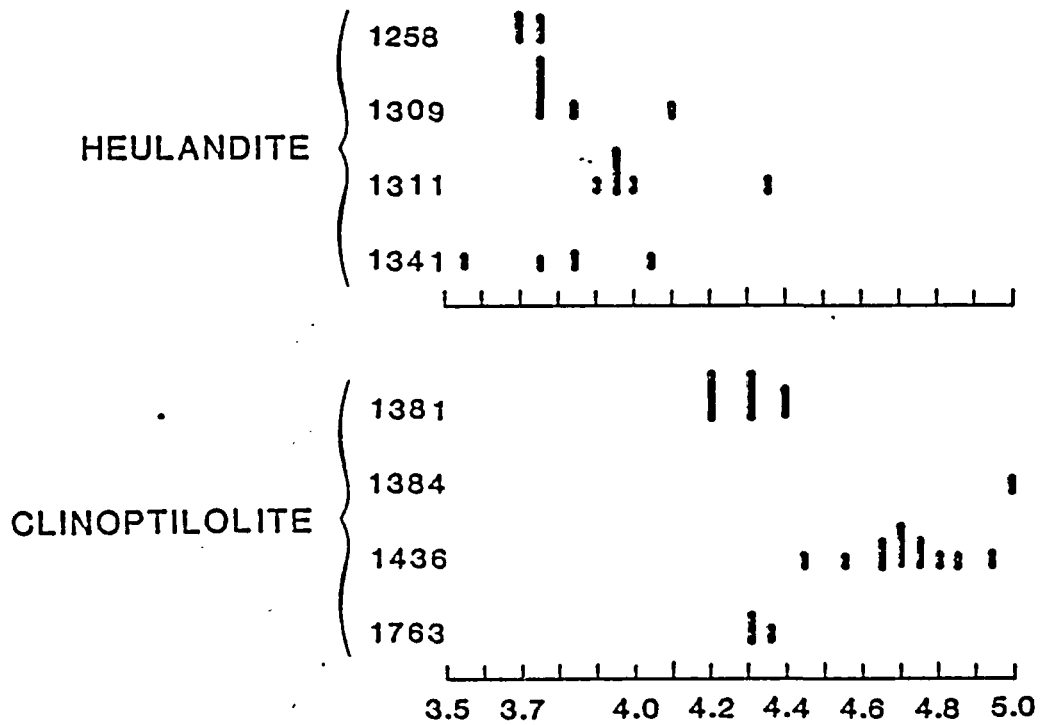

Fig. 47.
Si:Al ratio in clinoptilolites and heulandites lining fractures, USW G-4. Numbers in vertical column are sample depths.

devitrified tuff above and the zeolitized tuff below. The coatings are heulandite and mordenite, as in the devitrified tuff, but are much finer grained. Smectite is a major constituent in some of these fractures. Levy (1983) concluded that alteration within the vitrophyre was related to devitrification at the top of the vitrophyre and along fractures and therefore was related to the initial cooling of the tuff; however, most of the rock is unaltered.

In zeolitized nonwelded tuff in the lower Topopah Spring Member of the Paintbrush Tuff and in the Tuffs of Calico Hills, fracture mineralogy more closely resembles the secondary minerals in the whole rock. This zone of zeolitic tuff above the water table is part of zeolitic interval II (Bish et al., 1983) and is the highest occurrence of clinoptilolite in both the fractures and the whole rock in drill hole USW G-4. The fracture-filling clinoptilolite is microcrystalline (0.01-0.02 mm) in the zeolitized,

nonwelded Topopah Spring Member and in the bedded tuff beneath it. Although clinoptilolite is a major fracture mineral down to the SWL, throughout most of the Tuffs of Calico Hills and units below it is cryptocrystalline, producing a sharp XRD pattern, but visually identifiable only on SEM images. Although the compositions vary (with a possible trend toward more sodium with depth), all clinoptilolite analyzed plots on the potassic and sodic side of the Ca-K-Na ternary diagram (Fig. 44) whereas all heulandite is calcic, some with as much as 1.3 wt% (25 cation % Mg) MgO. The difference in Si:Al ratios (Fig. 47) appears consistent; the Si:Al ratio is lower for heulandite than for clinoptilolite. No mordenite occurs in the fractures or whole rock above ~1500 ft in the Tuffs of Calico Hills.

Smectite is a major fracture-filling mineral immediately above the SWL. As in the vitrophyre, the clays are randomly interstratified, dioctahedral smectite/illite with at least 75% smectite layers. The small sample sizes gave poorly defined XRD peaks so the exact amount of smectite could not be determined.

V. Summary of Fracture-Mineral Paragenesis and Discussion

Within the unsaturated zone in drill hole USW G-4 fracture-lining minerals that formed in several different regimes can be recognized. The types of fracture linings deposited change with time from lithophysal minerals to zeolites to smectite, but there is also a change in mineralogy with depth. Fractures in densely welded devitrified tuff, in vitric material, and in zeolitized nonwelded tuff contain different minerals as well as different morphologies of the same minerals (Fig. 48). One would not necessarily expect fractures in the Tuffs of Calico Hills to contain the same minerals or even the same sequence of minerals as those in the Topopah Spring Member of the Paintbrush Tuff because they are different eruptive units, and fractures within the Tuffs of Calico Hills may have formed and been mineralized before deposition of the Paintbrush Tuff. However, a more significant break in fracture mineralogy apparently occurs between heulandite and clinoptilolite at the top of the nonwelded zeolitic tuff in the Topopah Spring Member, rather than at the stratigraphic break between the Tuffs of Calico Hills and the Topopah Spring Member.

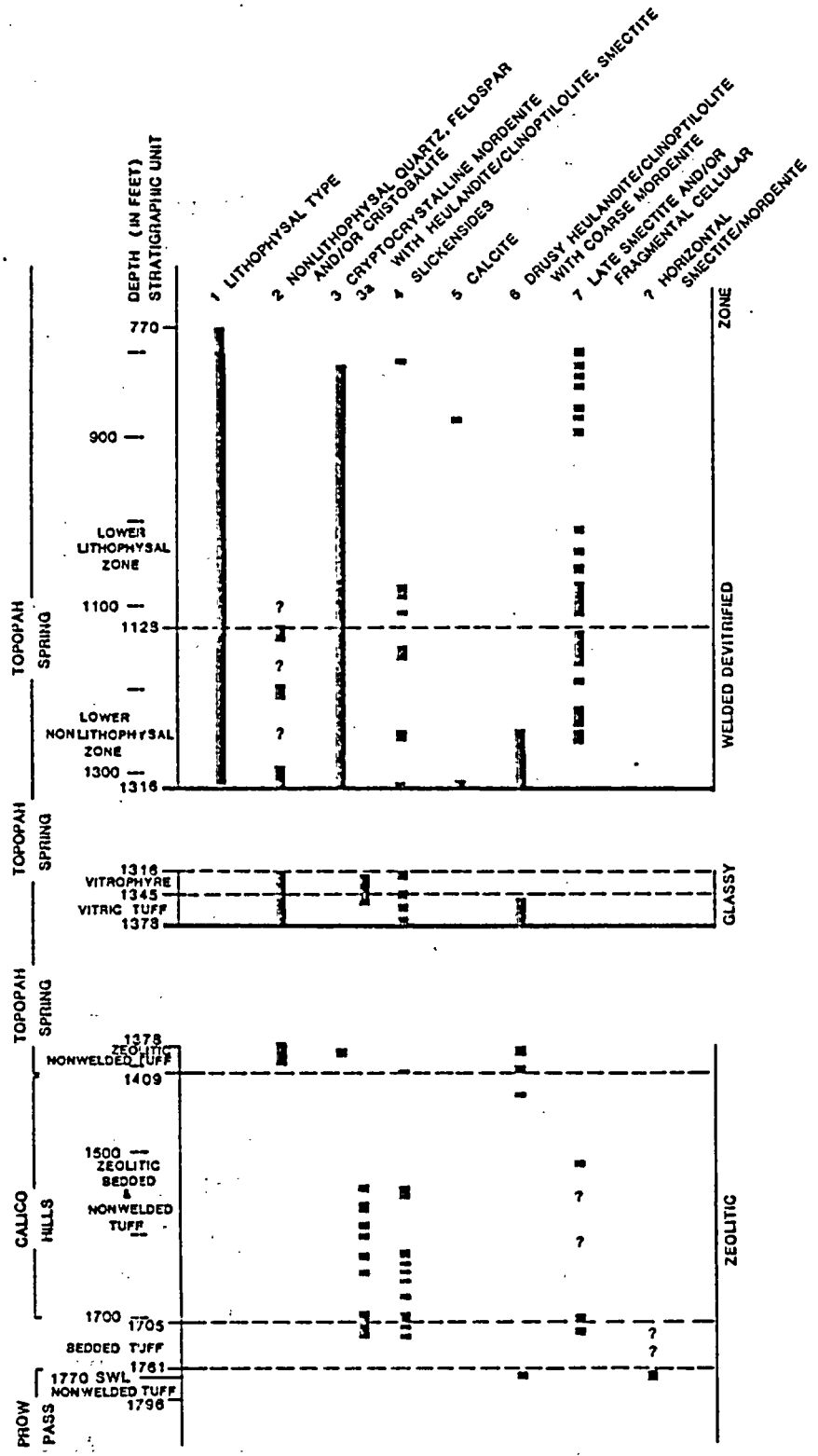

Fig. 48.
Sequence of fracture coatings in the unsaturated zone of USW G-4. Columns 3 and 3A are both cryptocrystalline; 3 is mordenite only, 3A is mordenite with other minerals.

In the densely welded, devitrified Topopah Spring Member, lithophysal-type fractures were the first formed and filled. Their mineralogy and relationship with and similarity to the lithophysae suggest that these fracture fillings were probably the result of vapor-phase crystallization and migrating high-temperature fluids during early cooling and devitrification of the tuff. The relationship of cristobalite-lined fractures to the lithophysal fractures is not known. Cristobalite predates mordenite, thus it also formed relatively early in the fracture-filling sequence of the Paintbrush Tuff.

Apparently enough time elapsed before cryptocrystalline (waxy) mordenite was deposited for some lithophysal fractures to seal and for new, crosscutting fractures to form. In other lithophysal fractures, mordenite coats the quartz and feldspar and obviously postdates them. Calcite occurs in few intervals in the unsaturated zone. Immediately above the vitrophyre, calcite postdates cristobalite and mordenite.

Movement causing visible slickensides in some fractures occurred after the fine-grained mordenite deposition. Slickensides do not occur on the calcite, but the calcite does have a strong preferential cleavage that may result from movement along the fracture.

Drusy heulandite and coarse mordenite (cobweb-like masses rather than waxy patches) were deposited in some of the fractures containing slickensides. These coarse-grained zeolites probably postdate major tectonic movement because they appear unaffected by slickensides. Smectite rosettes and cellular crusts of quartz and alkali feldspar fragments (mode of deposition unknown) postdate zeolite formation in these fractures.

Fracture minerals in the glassy zone are unlike those above or below it. The minerals are mostly very fine grained, as in the zeolitic zone below, but the zeolites are heulandite and mordenite, as in the devitrified zones above. Smectite is more abundant in this zone than in any other, except just above the water table. Levy (1984) concluded that the smectite-heulandite alteration and fracture filling in the vitrophyre may have occurred during late-stage devitrification of the Topopah Spring Member of the Paintbrush Tuff. If so, these minerals predate other zeolitization in the Topopah Spring Member. With the exception of one sample at the top of the lower lithophysal zone, smectite is abundant above the Prow Pass Member only in the vitrophyre and upper vitric zone, suggesting that conditions

during deposition of fracture minerals in this interval were different than they were in fractures in the intervals above and below it.

Identifying the sequence of fracture-lining events in the vitric zones is difficult. In the vitrophyre, all coatings are cryptocrystalline and are visually unidentifiable, but XRD analyses of the different layers indicate a sequence of primarily heulandite and cristobalite, with some smectite; primarily smectite, with heulandite; and primarily heulandite, with mordenite. In the vitric tuff below the vitrophyre, the minerals are visually unidentifiable. The morphology observed in SEM images does not correspond with the XRD patterns. Analyses by XRD indicate heulandite (1350 ft) and heulandite with mordenite (1362 ft).

As the host rock changes with depth in drill hole USW G-4 from nonwelded vitric tuff to nonwelded zeolitic tuff (zeolite interval II of Bish et al., 1983), the fracture-filling zeolite becomes clinoptilolite rather than heulandite as in the tuffs above the zeolitic zone. Based on SEM images, mordenite apparently postdates clinoptilolite where the two occur together. A second generation of clinoptilolite postdates the mordenite or is deposited directly on the original clinoptilolite where there is no mordenite in the fracture. Evidence suggests that fracture linings in this interval formed under different conditions from those for fracture linings in the unzeolitized tuffs. Mineralogy and grain size of fracture minerals in this zone are different from those in the zones above, and fracture mineralogy closely resembles the groundmass alteration in this zone.

Hoover (1968) and Moncure et al. (1981) have discussed the formation of zeolites in tuffs at the Nevada Test Site. Hoover (1968) favors an open system with a chemical gradient, ponding of water above impermeable zones, and temperatures near the present gradient. Moncure et al. (1981) believe the zeolites formed in a closed system (presumably below the water table) with virtually no transport of elements in or out of the tuff units and that zeolitization occurred at somewhat elevated temperatures soon after the tuffs formed and a water table was established. Both Hoover (1968) and Moncure et al. (1981) are looking at rock alteration in which water reacts with vitric material to form zeolites in place. The zeolites in the fractures are precipitation minerals. Little or no reaction occurs with grains of the host rock intersected by the fractures.

Zeolites occur only in fractures throughout most of the devitrified zone, with the exception of a 16-ft (5-m) interval immediately above the vitrophyre, where heulandite occurs in the whole rock. A 60-ft-thick, glassy zone beneath the devitrified zone is mostly unaltered (except in and near fractures). The presence of nonwelded vitric tuff in this zone suggests that it has never been below the water table. Because the fracture-coating zeolites are different above and below this glassy zone, they must have formed from different solutions. The microcrystalline zeolites in fractures above the zeolitic-tuff zone were probably formed by water moving through fractures in unsaturated tuff in an open hydrologic system. The host tuff is unaltered, even where it is vitric, and there is no evidence of ponding (a perched water table), except possibly in the lower 16 ft (5 m) of the devitrified zone. Only within the zeolitic tuffs of the unsaturated zone are the fracture linings and rock-alteration minerals similar, and therefore possibly deposited from the same fluids. In drill hole USW G-3 clinoptilolite is present in the rock matrix (in the Prow Pass Member of the Crater Flat Tuff) ~630 ft above the present SWL (Vaniman et al., 1984). Clinoptilolite at that depth could be attributed to a paleo water table relatively higher than the present one (for example, the water table was higher or the rock mass was lower). Similar zeolitization in the host rock and in the fractures of zeolitic interval II from USW G-4 suggests similar conditions of formation, (that is, water throughout the entire rock unit and not just in the fractures). Near-total saturation presently occurs in some units well above the zeolitic zone (Scott et al., 1983), yet the only other zone of host-rock zeolitization (and it is minor there) is just above the vitrophyre, where water may also have accumulated and moved more slowly than in the devitrified zones above. Therefore, zeolite formation below the paleo water table seems to explain the similarity of rock-matrix alteration and fracture minerals (and their continuity across lithologic formations). Figure 44 shows the similarity in chemical composition between the fracture minerals and host-rock alteration below 1432 ft. The vitric unit above the lower zeolitized Topopah Spring Member is nonwelded and, if the saturated conditions under which zeolite formation occurred were caused by capillary action rather than by a higher water table, it is difficult to explain the break within the nonwelded base of the Topopah Spring Member. The origin of

the chlorides at 1721 ft and their relationship to the fracture zeolites in this interval are not known.

One exception to the apparent uniformity of mineral chemistry within the zeolitic unsaturated zone is the microcrystalline clinoptilolite at 1763 ft in the upper Prow Pass Member. This clinoptilolite is markedly lower in K and higher in Na than microcrystalline clinoptilolite higher up in the core (Table II and Fig. 44). This clinoptilolite may represent an earlier episode of zeolitization (it occurs in an older tuff unit), but because this study did not continue below the SWL, it is not yet known if there are similar occurrences deeper in the core. Studying the saturated zone (that is, below the SWL) will determine whether the present water table marks any difference in fracture mineralogy and whether a consistent change in the composition of fracture-lining clinoptilolite occurs with depth. Clinoptilolite in host-rock samples from drill hole USW G-4 is more calcic with increasing depth.*

Microscopic, blocky euhedral crystals of clinoptilolite in the lower Topopah Spring Member of the Paintbrush Tuff, upper Tuffs of Calico Hills, and upper Prow Pass Member of the Crater Flat Tuff have morphology similar to the heulandite in the devitrified zone and therefore may have formed under similar conditions (above the water table). All coarsely crystalline clinoptilolite may not have formed during the same zeolitization episode, and the lower occurrence (1763 ft) may even have formed before deposition of the Topopah Spring Member. Cryptocrystalline coatings fill most of the fractures in the zeolitic host-rock interval, and, except for the abundance of smectite in horizontal fractures in the Prow Pass Member, closely resemble the whole rock alteration; all these coatings may postdate the microcrystalline clinoptilolite seen in the sample from 1763 ft. However, the crosscutting relationships to verify this occur only in the horizontal disk fractures at the top of the Prow Pass Member.

VI. Conclusions

Fracture-lining minerals in tuff may be very different from minerals in the surrounding rock matrix. In the unsaturated zone of USW G-4, the

*Information provided by D. Broxton, Los Alamos National Laboratory, (1984).

fracture mineralogy varies greatly with the nature of the host rock (devitrified, glassy, or zeolitized). The differences between host-rock and fracture mineralogy are greatest in the devitrified and glassy units.

In the devitrified zone, the earliest fracture-filling minerals are quartz and feldspar, which occur in fractures connected with lithophysae. Mordenite, the earliest zeolite formed in fractures, occurs over the entire interval sampled in the devitrified zone. Some mordenite-lined fractures crosscut earlier, sealed quartz-feldspar fractures. Manganese oxides/hydroxides usually occur with or just beneath the mordenite. The single calcite fracture sampled crosscuts some mordenite-lined fractures. Slickensides striate mordenite and manganese oxides in many fractures. Heulandite and coarse mordenite that occur in fractures from 1245 ft to 1315 ft are not slickensided. Small smectite clusters and fragments of quartz and feldspar (possibly tuff pulverized during coring) coat all other fracture minerals.

In the glassy zone (including the vitrophyre and nonwelded vitric tuff) the zeolites are heulandite and mordenite, but they are fine grained and visually unidentifiable. Smectite accompanies the zeolites in some fractures. Zeolites in fractures in the devitrified and glassy zones thus occur at much shallower depths than in the host rock.

From the zeolitic zone in the nonwelded Topopah Spring to at least the top of the Prow Pass Member (SWL at 1770 ft) fracture mineralogy is similar to the host-rock alteration. This zone may once have been below the SWL.

ACKNOWLEDGMENTS

The author wishes to thank Fred Mumpton and Dave Broxton for critically reading and suggesting improvements in the manuscript.

References

Bence, A. E. and A. L. Albee, 1968, Empirical correction factors for electron microanalysis of silicates and oxides. J. Geol., 76, 382-403.

Bish, D. L., F. A. Caporuscio, J. F. Copp, B. M. Crowe, J. D. Purson, J. R. Smyth, and R. G. Warren, 1981, Preliminary stratigraphic and petrologic characterization of core samples from USW-G1, Yucca Mountain, Nevada. A. C. Waters and P. R. Carroll, eds., Los Alamos National Laboratory report LA-8840-MS (November 1981).

Bish, D. L., A. E. Ogard, D. T. Vaniman, and L. Benson, 1983, Mineralogy-petrology and groundwater geochemistry of Yucca Mountain tuffs. Materials Research Society 1983 Annual Meeting, Boston, Mass., November 14-17, 1983, 26, 283-291.

Boles, J. R., 1972, Composition, optical properties, cell dimensions, and thermal stability of some heulandite group zeolites. Am. Mineral. 57, 1463-1493.

Byers, F. M., Jr., W. J. Carr, P. Orkild, W. D. Quinlivan, K. A. Sargent, 1976, Volcanic Suites and related calderas of Timber Mountain-Oasis Valley Caldera Complex, Southern Nevada. US Geol. Surv. Prof. Paper 919.

Caporuscio, F., D. Vaniman, D. Bish, D. Broxton, B. Arney, G. Heiken, F. Byers, R. Gooley, and E. Semarge, 1982, Petrologic studies of drill cores USW-G2 and UE25b-1H, Yucca Mountain, Nevada. Los Alamos National Laboratory report LA-9255-MS.

Carr, W. J., F. M. Byers, Jr., and P. P. Orkild, 1984, Stratigraphic and volcano-tectonic relations of Crater Flat Tuff and some older volcanic units, Nye County, Nevada. US Geol. Surv. Open-file report 84-114.

Carr, W. J., 1974, Summary of tectonic and structural evidence for stress orientation at the Nevada Test Site. US Geol. Surv. Open-file report 74-176, 53 p.

Christiansen, R. L. and P. W. Lipman, 1965, Geologic map of the Topopah Spring northwest quadrangle, Nye County, Nevada. US Geol. Surv. Map GQ 444, scale 1:24 000.

Graham, J., C. R. M. Butt and R. B. W. Vigers, 1984, Sub-surface charging, a source of error in microprobe analysis. X-ray Spectrometry, 13(3), 126-133.

Hoover, D. L., 1968, Genesis of zeolites, Nevada Test Site. Geol. Soc. Am. Memoir 110, p. 275-284.

Levy, S. S., 1983, Studies of altered vitrophyre for the prediction of nuclear waste repository-induced thermal alteration at Yucca Mountain, Nevada. Materials Research Society 1983 Annual Meeting, Boston, Mass., November 14-17, 1983, 26, 959-966.

Levy, S. S., 1984, Petrology of samples from drill holes USW H-3, H-4, and H-5, Yucca Mountain, Nevada. Los Alamos National Laboratory report LA-9706-MS, (June 1984).

Lipman, P. W., R. L. Christiansen, and J. T. O'Connor, 1966, A compositionally zoned ash-flow sheet in southern Nevada. US Geol. Surv. Prof. Paper 524-F, 47 p.

Lipman, P. W. and E. J. McKay, 1965, Geologic map of the Topopah Spring southwest quadrangle, Nye County, Nevada. US Geol. Surv. Map GQ 439, scale 1:24 000.

Marvin, R. F., F. M. Byers, Jr., H. H. Mehnert, P. P. Orkild, T. W. Stern, 1970, Radiometric ages and stratigraphic sequence of volcanic and plutonic rocks, southern Nye and western Lincoln Counties, Nevada. Geol. Soc. Am. Bull. 81, 2657-2676.

Moncure, G. K., R. C. Surdam, and H. L. McKague, 1981, Zeolite Diagenesis below Pahute Mesa, Nevada Test Site, Clays and Clay Minerals 29(5), 385-396.

Mumpton, F. A., 1960, Clinoptilolite redefined. Am. Mineral. 45, 351-369.

Scott, R. B., R. W. Spengler, S. Diehl, A. R. Lappin, and M. P. Chornack, 1983, Geologic character of tuffs in the unsaturated zone at Yucca Mountain, southern Nevada: in J. W. Mercer, P. S. L. Rao and I. W. Irvine, Eds. Role of the Unsaturated Zone in Radioactive and Hazardous Waste Disposal: Ann Arbor Science, Ann Arbor, Michigan, p. 289-335.

Spengler, R. W. and M. P. Chornack, 1984, Stratigraphic and structural characteristics of volcanic rocks in core hole USW G-4, Yucca Mountain, Nye County, Nevada, section on geophysical logs by D. C. Muller and J. E. Kibler. US Geol. Surv. Open-file report 84-789.

Vaniman, D., D. Bish, D. Broxton, F. Byers, G. Heiken, B. Carlos, E. Semarge, F. Caporuscio, and R. Gooley, 1984, Variations in authigenic mineralogy and sorptive zeolite abundance at Yucca Mountain, Nevada, based on studies of drill cores USW GU-3 and G-3. Los Alamos National Laboratory report LA-9707-MS, (June 1984).

☆USGPO: 1985-576-111/10050

Printed in the United States of America
Available from
National Technical Information Service
US Department of Commerce
5285 Port Royal Road
Springfield, VA 22161

Microfiche (A01)

Page Range	NTIS Price Code	Page Range	NTIS Price Code	Page Range	NTIS Price Code	Page Range	NTIS Price Code
001-025	A02	151-175	A08	301-325	A14	451-475	A20
026-050	A03	176-200	A09	326-350	A15	476-500	A21
051-075	A04	201-225	A10	351-375	A16	501-525	A22
076-100	A05	226-250	A11	376-400	A17	526-550	A23
101-125	A06	251-275	A12	401-425	A18	551-575	A24
126-150	A07	276-300	A13	426-450	A19	576-600	A25
						601-up*	A99

*Contact NTIS for a price quote.

Los Alamos